UiT
THE ARCTIC
UNIVERSITY
OF NORWAY

Department of physics and technology

Marine Radar Properties, Analysis and Applications

—

Kai Magne Kaspersen

Master thesis in Energy, Climate and Environment [EOM-3901] … August 2017

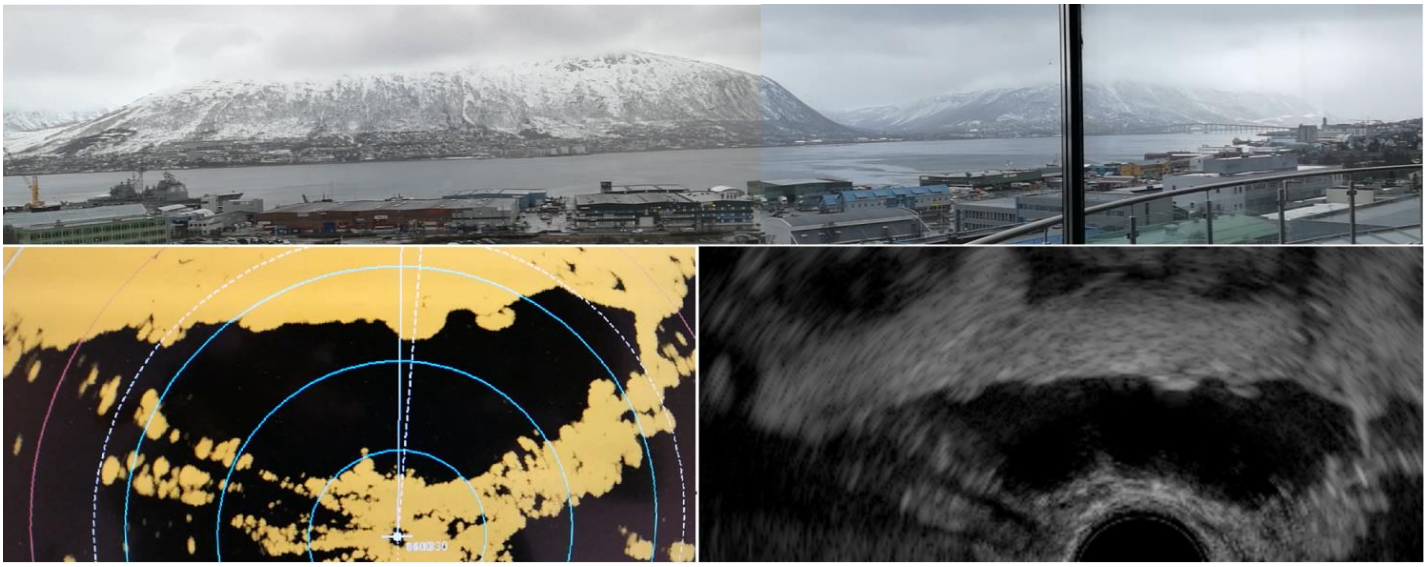

UNIVERSITY OF TROMSØ

Abstract

In this thesis marine radars are compared with synthetic aperture radars (SAR) and the possibility of cross-over applications are investigated. A first cross-over has been demonstrated by using the TS-CFAR on marine radar images. The TS-CFAR was originally developed for SAR and is a constant false alarm rate (CFAR) detection algorithm based on truncated statistics. Detecting weak targets embedded in sea clutter is difficult because it is hard to find a model describing the sea in its various conditions. For detection algorithms such as constant false alarm rate (CFAR) the accuracy of the sea clutter estimation directly relates to performance. A model comparison between Weibull-, Gamma-, Log-normal- and Rayleigh PDF on sea clutter data has been performed. Sea clutter data was separated at sectors at different range, and both low- and high resolution data from a X-band Sea-Hawk radar and S-band JRC JMR solid state radar was used in the comparison. Our results show that the Weibull PDF models the sea clutter best in most cases, but we found indications that the Gamma PDF fit the clutter best when texture is present. The TS-CFAR was compared to a CA-CFAR both with an underlying Weibull model and an underlying Gamma model. Our results show that TS-CFAR clearly performed best on high resolution data and for multiple target situations. This thesis also shows how to extract raw data from marine radars which proved to be a formidable task.

Acknowledgement

First and foremost, I wish to tank my supervisor at UiT - The Arctic University of Norway, and CIRFA - Centre for Integrated Remote Sensing and Forecasting for Arctic Operations, Dr. Anthony Doulgeris, whose encouragement, guidance and support from the initial to the final level enabled me to develop an understanding of the subject. He was truly able to give me the advice I needed and to motivate me when my spirits were down. I could not have imagined a better supervisor for my Master study. He has shown support in a number of ways, starting with helping me defining my subject, guidance with writing, and assistance whenever needed during the data collection and writing process. Next, I would like to thank my co-supervisor, Dr. Dagfinn Husjord at UiT. Without your marine contacts and support with the radars, my work would not have been possible.

I would also like to thank Ståle Antonsen at UiT, for the technical assistance, and help with installing the dspnor scan streamer. My thanks go to the Faculty of Science and Technology and the Department of Physics and Technology for funding my study trip to Bergen, and to the Department of Engineering and Safety for access to the JRC and Furuno radar. Additionally, I would like to thank, Dr. Ding Tao, for letting me use his Matlab code for the TS-CFAR. Without his effort a smooth delivery of the thesis would not have been possible.

My utmost gratitude goes to John Søreide and Morten Steinbakk at Sea-Hawk for inviting me to Bergen and providing us with invaluable radar data. You gave me tremendous help and guidance. Last but not least I would like to thank dspnor for providing us with the scan streamer which became an essential part of the project. My special thanks go to Geir Agdesteen and Lennart Dale, you truly helped me by providing me with software necessary to use our radar data.

Finally, I offer my regards to those who supported me in any respect during the completion of the project, most of all my family and friends.

Contents

Chapter 1

Introduction

Since the first time they appeared on commercial ships after the Second World War, radars have become an irreplaceable navigational instrument on the ship's bridge, especially for navigation during the night or in foggy conditions. The instrument sends out an electromagnetic microwave and receives its reflection with a slight time delay representing the distance to the reflected object. Not all of the reflections received by the radar are interesting for navigational purposes, and it might be difficult for the operator to distinguish ships from those that mess up or *clutter* the image. The general terminology is to name the reflections of interest *targets* and the reflections we want to remove from the system for *clutter*. Detecting targets in clutter has always been and still is a big challenge for radar designers. When the sea is calm it is generally not problematic to detect large ships, but when ships get smaller and the sea rougher, targets might be fully disguised in clutter and dangerous situations might develop. For such situations, the accuracy of the detection algorithm might be the difference of seeing an important target or not. There are many detection challenges beyond ship detection such as detecting small submerged icebergs, such as *growlers*, or detecting rocks or even kayakers - for their own safety! For an environmental point of view, better target detection can help reduce maritime disasters such as oil spillage from grounding ships, in uncharted territories, or ships colliding with icebergs. With the right applications even oil slicks can be detected on a marine radar, which might be beneficial for coast guards or to ships performing oil recovery operations. Such technology is already available especially in the synthetic aperture radar (SAR) community. SAR is radar satellites that are especially beneficial in polar regions because of their ability to see through clouds and in darkness. They are extensively used for ship detection and surveillance, and for studying ice and weather phenomenons, and for forecasting. If it is possible to transfer applications from SAR to marine radars, and opposite, this might open up several novel opportunities for both communities, or maybe just new thoughts.

In this thesis we will compare marine radars with SAR and check whether there could be cross-over applications. This we will do by checking the signal and statistical properties, and then we will go on and perform a first demonstration of such a cross-over by using the newly developed target detection algorithm developed by*Tao et al.* [1]. This is a new kind of constant false alarm (CFAR) algorithm that uses truncation to remove target pixels from the the clutter, in order to better decide a threshold for detection. Furthermore, the algorithm uses a truncated probability density model (PDF) to better estimate the clutter. Marine radars use a rotating directional antenna, and are therefore able to make an image of its surroundings by recording both antenna angle and time. The power of the received echo strongly depends on range, but also on the dielectric property and the size and shape of the reflecting medium. A surface made of metal returns a stronger reflection than a surface made of wood, e.g. a vessel made of metal returns a stronger echo than a vessel made of wood situated at the same range [2]. To separate different reflecting media in order of their reflecting ability, we say that a material with a strong reflection in the direction of the radar has a large radar cross section (RCS). Since the wavelength of a radar is in the order of centimetres and the spatial resolution is in the order of meters to tens of meters, each resolution cell in a radar can be thought of as a sum of many individual scatterers [3]. A small target sharing a resolution cell with scatterers defined as clutter might therefore be difficult to detect, especially if the radar cross section of the target in itself is weak. For these reasons the strength of the target echo might be very similar to the resolution cells nearby containing only clutter, and it might be difficult for the naked eye to distinguish them. This thesis will as well as demonstrating the TS-CFAR and performing a model comparison, summarize different detection algorithm used in marine systems today to be able to better distinguish *target* cells from *clutter* cells. A comparison will be performed between what we consider to be the most conventional CFAR, the CA-CFAR, and the newly developed TS-CFAR. First, background theory necessary for this thesis will be summarized and the marine radar system will be described.

Chapter 2

Radar Theory

2.1 Radar Basics

To explain the radar basics it helps to visualize the transmission of an ideal square wave pulse as described in figure 1 a). Ignoring any attenuation effects, the reflection of the square wave pulse on a point target will be a convolution of the original pulse with a slight time delay as described in figure 1 b) [4]. The time delay represent the range to the point target, and since we know that the velocity of the electromagnetic wave is approximately the speed of light c, we can find the distance to the point target. Theoretically we know that the attenuation effect, excluding loss factors, for the pulse is governed by the radar equation listed below [5], and will thus attenuate proportional to $1/R^4$.

$$P_r = \frac{P_t G_t G_r \lambda^2 \sigma}{(4\pi)^3 R^4} \tag{1}$$

Here P_r is the power received, P_t is the transmitted power, G_t and G_r are the gain factors for the transmitting and receiving antenna respectively, λ is the wavelength, σ is the radar cross section, and R is the radius centred in the radar. If we rearrange the equation a bit, we get the following form (equation 2), where the first term is the effective transmitted power per solid angle and per unit area, the second term is the reflected power (echo term) per solid angle and unit area, in the direction of the receiving antenna. The last term is the efficiency of the receiving antenna. The attenuation of $1/R^4$ therefore comes from the fact that both the transmitted beam and the backscatter attenuate in accordance with the solid angle for an ideal case.

$$P_r = \frac{P_t G_t}{4\pi R^2} \; \frac{\sigma}{4\pi R^2} \; \frac{G_r \lambda^2}{4\pi} \tag{2}$$

The actual pulses transmitted in radars are actually approximations of triangular pulses like figure 1 c) [6, 2], which will result in less interference effects. Although, if we include a layer of noise

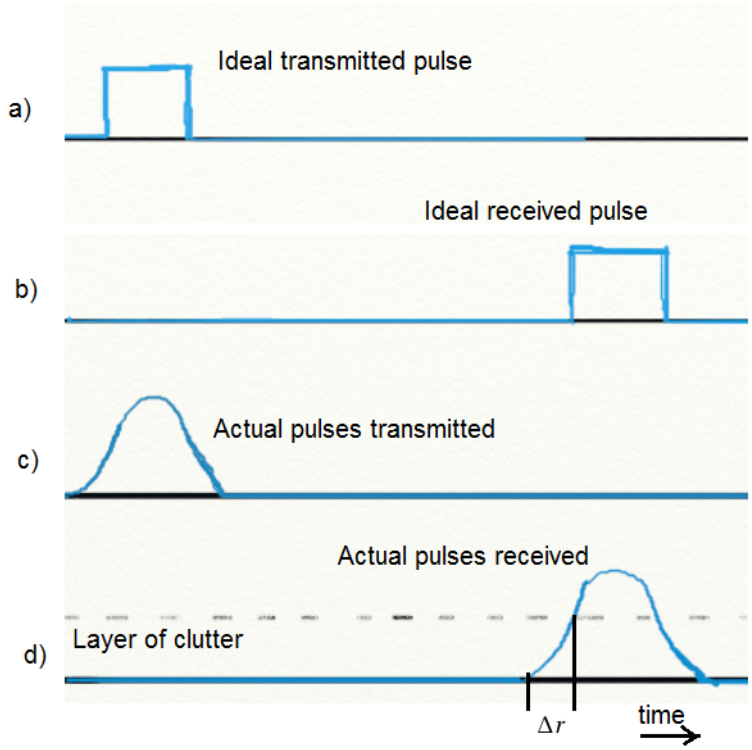

Figure 1: *a) Drawing of an ideal transmitted pulse. b) Drawing of an ideal received pulse, which is the convolution of the transmitted pulse with a time delay. c) Approximation of a triangular pulse d) Received actual pulse in a layer of noise. There will be a small range inaccuracy* Δr

as described in figure 1 d) we can see that a triangular pulse will result in a slight range inaccuracy Δr. The ability for the radar to discriminate between to separate point targets defines the spatial resolution of the radar. We differentiate between azimuth resolution and range resolution (see figure 6), where azimuth resolution depends on the beamwidth of the radar and the range resolution depends on the pulse length (τ) of the transmitted beam [2]. If the distance between two targets is less than the range resolution, the trailing edge of the pulse hitting the first target will be mixed with the leading edge of the pulse hitting the second target, and the two targets will for non-coherent radars not be discernible [7]. The range resolution for non-coherent radars is therefore:

$$\Delta r = \frac{\tau c}{2} \tag{3}$$

Here τ is the pulse length and c is the speed of light.

If the electromagnetic microwaves transmitted from the radar is coherent it is possible to separate two targets at any pulse length by using pulse modulation [2]. A radar is phase coherent if the phases of the transmitted waves are known, such that phases of the waves received can be directly compared with those transmitted [2, 8]. The motivation for using pulse modulation is to increase the signal to noise ratio (SNR) or the resolution when a limited amount of power is available. The

SNR is the ratio of received echo energy (E_r) to thermal noise (N). The maximum signal to noise ratio possible in a radar system is listed below [5]:

$$SNR_{max} = \frac{E_r}{N} = \frac{E_t G_t G_r \lambda^2 \sigma}{(4\pi)^3 R^4 k T L} \tag{4}$$

This equation is recognized as the ratio of the radar equation given in equation 1 to thermal noise, which is defined as $N = kT$, where $k = 1.38 \times 10^{-23} J/K$ is the Bolzmann's constant and T is the thermal noise equivalent temperature. Furthermore, L is the loss factors and $E_t = P_t \tau$ is the transmitted energy. The signal to noise ratio can thus be increased by either increasing the transmitted power or increasing the transmitted pulse length. The most common pulse modulation used is linear frequency modulation which is also known as chirp modulation [7].

An electromagnetic wave can be described as a complex phasor, and the real part is defined as:

$$v(t) = \Re e\{A(t) e^{i(\omega_0 t + \phi)}\} = A(t)\cos(\omega_0 t + \phi) \tag{5}$$

The function: $\psi(t) = \omega_o t + \phi$, is called the the angle function [4], and if we let $\psi(t)$ be a quadratic function like:

$$\psi(t) = 2\pi\mu t^2 + 2\pi f_0 + \phi \tag{6}$$

the derivative ($\frac{\partial}{\partial t}$) of the angle function change linearly with time. Quadratic functions like equation 6 are known as chirps [4]. If the transmitted signal of a radar is:

$$v(t) = A(t)\ \exp\left[2\pi i\left(f_c t + \frac{K t^2}{2}\right)\right] \tag{7}$$

where $A(t) = 1$ for $-\tau/2 \leq t \leq \tau/2$ and equals 0 otherwise, f_c is the center frequency, and K is the chirp rate [8]. The corresponding instantaneous frequency is:

$$f(t) = \frac{1}{2\pi}\frac{\partial}{\partial t} 2\pi\left(f_c t + \frac{K t^2}{2}\right) = f_c - K t \tag{8}$$

for $-\tau/2 \leq t \leq \tau/2$. The signal bandwidth is defined to be $B = K\tau$ [8]. We can see that the instantaneous frequency changes linearly with time within the bandwidth, and that the signal therefore is a chirp. If we transmit our signal at $t = 0$, and we receive an echo signal from a point target at a distance R at time $t_R = 2R/c$, then the received signal can be expressed as:

$$v_R(t) = \alpha\, v(t - t_R) \tag{9}$$

Here $v(t - t_R)$ is the transmitted signal with a time delay (at distance R), and α is the attenuation of the propagating wave, which also includes the effect of the radar cross section [8]. By convolving

the complex conjugate of the transmitted signal with the received signal we get our matched filter output:

$$v_o(t) = \int_{-\infty}^{\infty} v^*(\zeta - t)\, v_R(\zeta)\, d\zeta \tag{10}$$

In real radar systems the fast fourier transform (FFT) is used to transform the signal to the frequency domain. Then the signal is multiplied with the filter, and afterwards transformed back to the time domain, again by using the inverse fast fourier transform (IFFT) [8]. It is well known that convolution in time domain corresponds to multiplication in frequency domain [4]. The reason for using FFT is because performing multiplication uses much less processing power in a computer than performing convolution [8]. The solution to the convolution in equation 10 is:

$$v_0(t) = \alpha\tau \ \exp(i2\pi f_c t) \ \exp(-i4\pi R/\lambda) \frac{\sin\left[\pi K(t - t_R)(\tau - |t - t_R|)\right]}{\pi K\tau(t - t_R)} \tag{11}$$

for $(t_R - \tau) \leq t \leq (t_R + \tau)$

The first term is just the carrier frequency, and this will be filtered out [8], and by replacing t_R with $2R/c$, α with E_R which is the electromagnetic field of the point source, and by using the approximation for $|t - t_R| << \tau$, we get: [7, 8]

$$v_0(t) = E_R\tau \ \exp(-i4\pi R/\lambda) \frac{\sin\left[\pi K\tau(t - 2R/c)\right]}{\pi K\tau(t - 2R/c)} \tag{12}$$

for $(2R/c - \tau) \leq t \leq (2R/c + \tau)$

The half-power points can be found by solving:

$$\frac{\sin^2\left[\pi K\tau(t - 2R/c)\right]}{\pi K(\tau(t - 2R/c))^2} = \frac{1}{2} \tag{13}$$

The solution to this equation gives a half-power time width of:

$$\Delta t \approx \frac{2.8}{\pi K\tau} \tag{14}$$

This is only valid if the time-bandwidth $K\tau$ is much larger than $2.8/\pi$. The physical boundary for the minimum distance two point targets can be discriminated to each other is given by the Rayleigh criterion [8]. The smallest separable distance is when the maximum diffraction of one point meets the minimum diffraction (first null) to the second point [8]. By using equation 11 it is possible to show that this limit is given by

$$\pi K\tau \Delta t_{min} = \pi \tag{15}$$

Since $K\tau$ is the same as the bandwidth B, the minimum time resolution Δt_{min} is:

$$\Delta t_{min} = \frac{1}{B} \tag{16}$$

Substituting Δt_{min} with τ in equation 3 , results in the following equation for the range resolution for coherent radars using chirp modulation:

$$\Delta_{r(chirp)} = \frac{c}{2B} \tag{17}$$

Unless the coherent radar takes advantage of the phase difference, the azimuth resolution for coherent radars is the same as for non-coherent radars and dependent on the antenna pattern. The width of the antenna pattern and the corresponding beamwidth is dependent on the length of the radar antenna [7, 2]. For a simple linear array with uniform amplitude the antenna pattern is given by [8]:

$$F(\theta) = \left| \frac{\sin\left(\frac{kL}{2}\sin(\theta)\right)}{\frac{kL}{2}\sin(\theta)} \right|^2 \tag{18}$$

Here θ is the direction of the antenna beam, L is the length of the antenna array and k is the wavenumber. The beamwidth β for a radar system is often chosen to be the halfpower of the main lobe of the antenna pattern, which is defined as being the angle on each side of the lobe where the power is half the total power. By solving equation (18) numerically for $\theta = \beta/2$ and $F(\beta/2) = 0.5$, the angle is found to be $\beta = 0.88\,\lambda/L$, which can be approximated to be

$$\beta \approx \frac{\lambda}{L} \tag{19}$$

for wavelengths much smaller than the antenna length L [8].

2.2 Marine radar

Almost all marine radars transmit in very short pulses in order to increase the spatial resolution, or in other words, the minimum separation distance between two *targets*. Additionally, transmitting in short pulses reduces the bandwidth for the transmission and thereby also the interference with other systems, including other radars. The radar will receive reflections, or echoes, from everything within the maximum range of the system. The maximum range depends on the power of the radar, but also the height of the radar above sea level and atmospheric conditions. This is because the upper range limit is restrained by the curvature of the earth, and the microwaves might bend when interacting with the atmosphere in special conditions. [2, 6] Because of safety by redundancy, every vessel larger than 3000 gross tonnage (GT) is required by the International Maritime Organization (IMO) to be equipped with two independent radars. One of them must be a X-band radar ($\lambda \approx 3$ cm., $\nu \approx 9.4$ GHz), and the other radar is often chosen to be a S-band radar ($\lambda \approx 10$ cm., $\nu \approx 3$ GHz) [9]. Since X-band radars transmit electromagnetic waves with shorter wavelengths

than S-band radars they achieve radar images with greater resolution. The downside is that they receive more reflections from the sea and from precipitation than S-band radars and will therefore receive more clutter [2, 10].

The electromagnetic microwaves are transmitted in pulses with a pulse repetition frequency (PRF) of 500-3500 Hz from a directional antenna. Marine radars are equipped with a rotating antenna that sweeps around with a more or less constant frequency [10, 2]. For this reason the radar display is naturally represented in polar-coordinates. Each pulse is sampled and divided in increments of increasing range defining the range resolution. The azimuth resolution depends on the angular velocity of the antenna and the pulse repetition frequency (PRF) [2]. Due to wind and other contributing factors, the angular velocity will in reality be variable, which means that the azimuth resolution is not sampled at a precisely fixed interval in time [2], but the system receives a signal from the antenna azimuth encoder defining the current antenna azimuth angle [11]. The typical angular velocity of the antenna is about 20 to 60 rounds per minute (RPM) [10], but must be minimum 12 RPM according to SOLAS (40 RPM for high speed vessels) [9]. The PRF for a marine radar will have typical values from about 600 Hz to 3500 Hz, but the actual value depends on the selected range scale. The operator is able to change the preferred range on the radar, and most radars use a variable PRF that changes automatically with chosen range [10]. The reason for changing the PRF is because even though a high PRF is preferred for better azimuth resolution, the radar must receive the reflected pulse before transmitting a new one to avoid ambiguities [10]. To increase the maximum range of the radar the PRF is therefore reduced when long range display is chosen by the operator. Most marine radars use a magnetron oscillator and are thus non-coherent, but coherent solid state radars are recently getting affordable for ship owners and will most likely be more common in the future [2]. The range resolution for marine radars are therefore given by equation 3 and equation 17 for non-coherent and coherent radars respectively. The azimuth resolution depends on the PRF, the rate of the antenna rotation and the horizontal beamwidth, and is decreasing from increasing range as shown in figure 6. Each target should be hit by about 6 to 10 pulses such that the receiver receives a strong enough echo for the system to separate it from clutter [11, 10].

2.3 Synthetic Aperture Radar

Synthetic aperture radars (SAR) are used on many of the satellites used for remote sensing, but are also used on surveillance aircrafts. The difference between SAR and real aperture radars is that on SAR the movement of the aperture platform is used to synthesize a larger antenna and is therefore

able to greatly improve the azimuth resolution. For real aperture radars the resolution is limited by the azimuth beamwidth [7]. As the aperture moves along its flight track the amplitude and phase of the returned signal are stored. The larger antenna is synthesized by combining the successive returns and by comparing the phase-shifts of each return to a reference, which is a stable oscillator in the aperture [8]. The requirement is therefore that the phase-shift of the returned signal can be compared to the phase of the transmitted signal which means that the radar needs to be coherent [7, 8]. Both the SAR and real aperture radar system is visualized in the following figure (2), and also includes the general terminology.

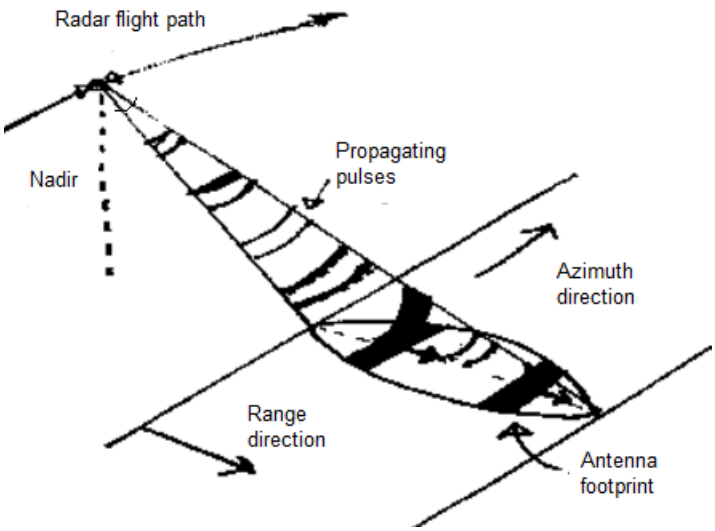

Figure 2: *Drawing of a SAR- or real aperture radar satellite. Swath, or the antenna footprint, is the terminology used for the area illuminated by the radar which depends on the horizontal- and vertical beamwidth*

The range (across-track) resolution is given by equation 17, except that now the look-angle θ must be accounted for. The smallest distance two targets can be separated in range is therefore [8]:

$$\Delta_{\mathrm{r(SAR)}} = \frac{c}{2B \sin \theta_i} \tag{20}$$

Here θ_i is the incident look-angle for this particular range distance, and is assumed very small. By this assumption $\Delta_{\mathrm{ground}} \approx \Delta_{\mathrm{slant}} \sin \theta_i$. This equation does also assume a flat and even ground surface. SAR and real aperture radars are side-looking, and the reason for this is to avoid ambiguities in the radar image caused by symmetry for distance measures on the right and left side of nadir [8]. If the look-angle were at nadir, each time delay would return two independent radar echoes, one from each side of nadir. The largest antenna length that can be synthesized in a SAR is determined by the footprint of the antenna pattern on the ground (the main lobe) [8]. The width of the main lobe (β_{main}) is $2\lambda/L$ and is solved by finding the distance to the first null of the antenna pattern of the particular antenna, see equation 18. The footprint depends on the distance of the aperture

over ground, which is $R = h/\cos\,\theta$, where R is the slant range and h is the height of the aperture over ground (at nadir). We get the following equation for the maximum length of the synthesized antenna:

$$L_{\text{synt}} = R\beta_{\text{main}} \approx \frac{h\beta_{\text{main}}}{\cos\,\theta} = \frac{2h\lambda}{L\,\cos\,\theta} \tag{21}$$

By substituting the synthesized antenna length into equation 19 we get:

$$\beta_{synt} \approx \frac{\lambda}{L_{synt}} = \frac{L\,cos\,\theta}{2h} \tag{22}$$

The best possible azimuth resolution is as mentioned the width of the beamwidth. The best possible azimuth resolution using the synthesized beamwidth is therefore:

$$\Delta_{\text{az(SAR)}} \approx R\beta_{\text{synt}} \approx \frac{h}{\cos\,\theta}\frac{L\cos\,\theta}{2h} = \frac{L}{2} \tag{23}$$

This approach is called the unfocused SAR. If we take into account the fact that the slant range (R) to the target is changing and is different for all the successive scatter returns it is possible to show that we get a synthesized array that is [8]:

$$L' = \sqrt{\frac{\lambda R}{2}} \tag{24}$$

This is called the focused SAR and has the following resolution which is, unlike the unfocused SAR, dependent on the range from the aperture to the surface. The resolution for the focused SAR is [8]:

$$\Delta'_{\text{az(SAR)}} = \sqrt{2\lambda R} \tag{25}$$

Below is an example of a SAR image of the Gulf of Finland the 9th of June 2017 at 10 am, captured by Copernicus Sentinel-1B. Ships are identified as bright dots, sometimes shaped like stars because of their strong radar cross section.

2.4 Statistical Distribution of Clutter

In the subsequent section, a description of clutter will be given, the origin of clutter, and the statistical distribution of different clutter types. For navigational purposes obvious targets are ships, navigational marks, and land and ice. Examples of *clutter* are snow, rain, and sea echo. Interesting *targets* may be hidden within the *clutter*, which is the reason why it is so important to find a good statistical distribution to describe it. A small improvement in describing the *clutter* might be the difference between detecting a weak *target* or not. To further specify the origin of the clutter, it

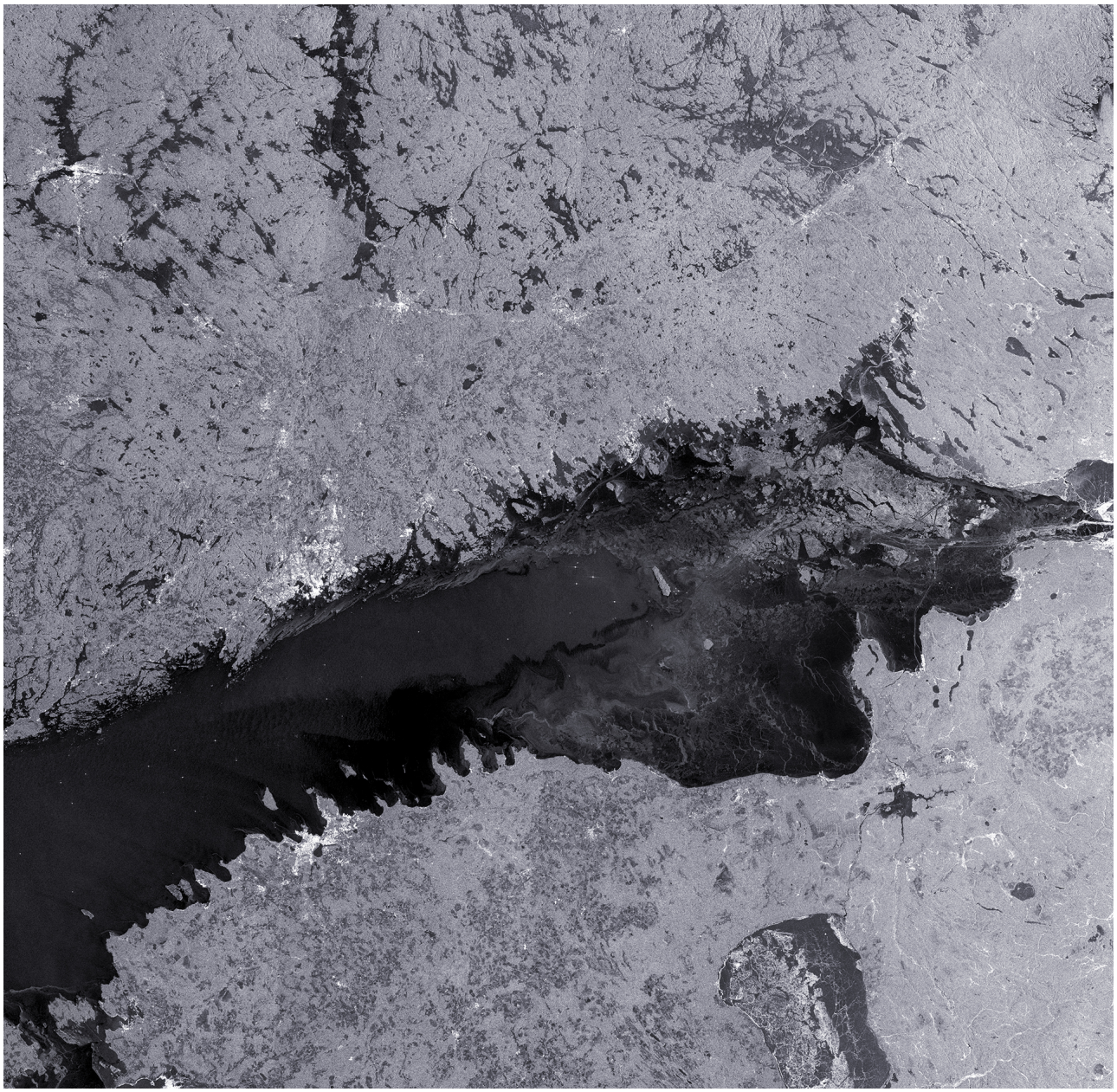

Figure 3: *SAR image of the Gulf of Finland the 9th of June 2017 at 10 am, captured by Copernicus Sentinel-1B. Ships are identified as bright dots, sometimes shaped like stars because of their strong RCS. Photo:ESA*

is common to give it a name, such as *sea clutter* or *rain clutter*. The intensity of the *sea clutter* increases as the weather gets rougher, such as when the wind speeds increase and waves become larger and more chaotic. This will be explained in detail in the following section. Small *targets* might actually be hidden behind large waves. Modern marine radars use algorithms to suppress sea and rain *clutter*, as well as integrating successive antenna sweeps to separate *targets* from *clutter*. This will be discussed in further detail in the following sections.

2.4.1 Thermal noise

In all electronics there is thermal noise originating from the fact that everything with a temperature above absolute zero contains vibrating or moving electrons [6]. Where there is a current such thermal noise is avoidable, be it in a semi-conductor, amplifier or a diode, and the radar needs to be able to detect a target in noise just as it has to detect a target in clutter [6]. The thermal noise sets a limit of how much power the radar can use in order to detect distant targets, which can be explained by looking at the signal-noise-ratio given in equation 4. There are several noise sources in a radar additional to thermal noise, but all can be combined to one total noise term since they are all fully random [6]. The noise follows the Gaussian distribution [6], and because sea clutter at low sea states and clutter from precipitation also can be modelled using the Gaussian distribution, the clutter for low sea states can be considered in the same way as thermal noise, but with added power [6]. For non-coherent radars, the Gaussian noise and clutter will be converted to the Rayleigh distribution when positively folded in the local oscillator (LO) [6].

2.4.2 The origin of sea clutter

Sea clutter is the reflection of the transmitted radar beam on the sea surface by tiny waves not larger than ripples on the ocean surface. These ripples are called capillary waves and are defined by the radar community as wavelengths in size up to a few centimetres [6]. Since the resolution cell is much larger than the wavelength of each individual capillary, the resolution cell can be thought of as a sum of the scatter contribution of many capillary waves [6]. The weak echoes received in the radar are almost random. As long as the number of capillaries, or scatterers, is large compared to the resolution cell, the scatterers will follow the central limit theorem and the received voltage will therefore be near-Gaussian distributed [6]. If ergodicity is assumed, the statistics of all resolution cells in the radar image can be compared to the statistics in one single resolution cell [12], such that the distribution of sea clutter under calm sea conditions when only capillary waves are present can then be assumed to also be near-Gaussian. When the sea is completely calm, almost

all of the transmitted beams are specularly reflected as shown in figure 4 a), and there will be little or no sea clutter. There will be more backscatter at high depression angles than low depression angles as will be explained in the next section. Following the Beaufort wind scale, capillary waves will appear the moment the wind is greater than 4 knots (sea state two), in other words as long as there is wind above the level of a breeze there will be capillary waves [6]. When capillary waves are present more of the transmitted beam will be backscattered as shown in figure 4 b), and the sea clutter will increase. This, we assume, is because the backscatter is frequently containing more of the specular part. Although, not directly explaining this assumption physically, this is confirmed by [6]. As wind is increasing, larger waves will appear which mariners call gravity waves [6]. The capillary waves will be superimposed on these larger waves, and the strength of the received sea clutter will increase for reasons that will become apparent in a moment. As figure 4 c) shows, the presence of gravity waves will locally, at facing wave fronts, increase the depression angle of the transmitted beam which will result in more backscatter [6]. Furthermore, forward reflection near wave troughs might multipath to the facing wave and further increase the amount of backscatter received in the radar. For low depression angles, and dependent on the size of the gravity waves, there will be a radar shadow by the wave crest opposite of the radar [6]. For large gravity waves relative to the spatial resolution of the radar, wave crests might occupy several resolution cells and might be identified as objects on the radar display [6]. The clutter will therefore have a textured appearance [3], and will no longer be fully random, which means that we expect a non-Gaussian distribution [6]. Because the inclination of the wave front is steeper if the radar is facing the wind than if the radar is looking down the wind, the sea clutter will have stronger returns upwind than downwind [6]. As the wind gets stronger and the gravity waves larger, the facing wave front will steepen resulting in more sea clutter. Although, the inclination of the wave front will not steepen beyond sea state five, and the received sea clutter will therefore stop increasing significantly for sea states higher than 5 [6]. If the sea is very rough and chaotic the wave crests get sharper and occasionally break and result in an increasing amount of so called sea spikes. This is a very steep wave front that will result in much backscatter. Such sea spikes might be falsely declared as targets by the detection algorithm implemented in the radar. Because of the fact that the sea spikes might appear on several successive scans, even the binary integrator might not be able to reject them [6]. This is because the binary integrator looks for a correlation between successive scans for the decision of discarding the information or not [6]. As the fluctuation of the gravity waves becomes larger, with longer wavelengths, it can be assumed that the sea clutter will be less Gaussian since the fluctuation occupies several resolution cells. It is known that a Log-normal distribution well describes the rough sea state with the frequent appearance of sea spikes, but this probability den-

sity distribution (PDF) is not able to describe both the calm sea state and the rough sea state and is therefore not practical [6]. The Weibull distribution is more flexible and can both describe the calm and rough sea states, and has frequently been used to model sea clutter in marine radars [13, 6]. In the SAR community, radar images assuming a constant RCS are often modelled using an Exponential distribution for a single look intensity (SLI) image and using a Gamma distribution for a multi looked intensity (MLI) image [3, 1]. The assumption of constant RCS is only valid for low sea states or for images with low resolution, in other words for images containing no texture [3]. When texture is present, as is the case for high resolution radar images of ocean in high sea states, the fluctuating RCS is often modelled using the Gamma distribution. The compound K-distribution has been suggested to describe clutter when texture is present, and will be briefly discussed in the following sections [14, 3]. See appendix A for more information about these distributions.

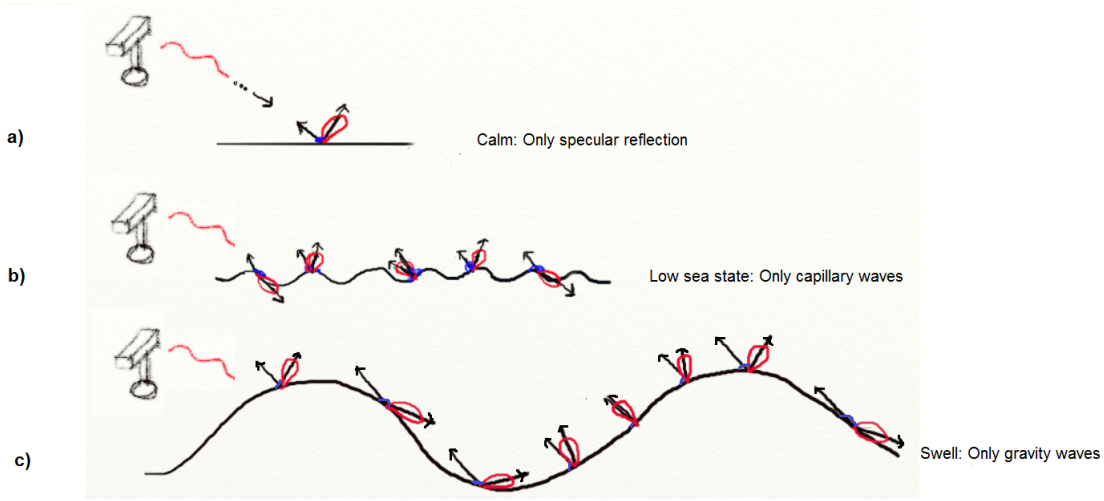

Figure 4: a) *The distribution of backscatter under calm sea state. b) The distribution of backscatter with capillary waves. c) The distribution of backscatter on swell without capillary waves.*

2.4.3 Speckle

Speckle is a phenomenon that occurs in coherent imaging systems such as SAR, laser or ultrasound. For that reason it is to be assumed that it also occurs in coherent marine radars. It looks like noise in an image, but since *speckle* is a part of the signal and does contain information, it is by definition no noise [3]. There would be no *speckle* if a resolution cell only contained one individual scatterer. It occurs when each resolution cell is a distribution of scatterers.

In order to understand *speckle* it is helpful to summarize how it is modelled. Below is the simple *speckle model* where each resolution cell is modelled as a discrete sum of individual scatterers

each with its own amplitude and phase.

$$A^{(mn)}e^{i\phi^{(mn)}} = \Sigma_{k=1}^{N} A_k e^{i\phi_k} \tag{26}$$

Here m and n are indexes for the amplitude and phase of the resolution cell at column m and row n of the image. A is the complex amplitude defined as $A = re^{i\theta}$, where r is the amplitude and the exponential is the initial phase. Equation (1) can be generalized to include j to M channels, and will then be defined as:

$$\begin{bmatrix} A_1 e^{i\phi_1} \\ . \\ . \\ . \\ A_M e^{i\phi_M} \end{bmatrix} = \Sigma_{k=1}^{N} \begin{bmatrix} r_{k1} e^{i\theta_{k1}} \\ . \\ . \\ . \\ r_{kM} e^{i\theta_{kM}} \end{bmatrix} e^{i\phi_k} \tag{27}$$

This model can be seen as a *random walk* in the complex plane where the phase is uniformly distributed between 0 and 2π. Because the amplitude and the phase will both add and destruct randomly we get interference which explains the noise-like pattern [3]. The *probability density function* (PDF) of the speckled backscatter depends on whether or not the number of scatterers N in the resolution cell is large enough for the *central limit theorem* (CLT) to be valid, that is $N \to \infty$. If the CLT is satisfied the in-phase ($A\ cos\ \phi$) and the quadrature($A\ sin\ \phi$) component will be Gaussian distributed with zero mean, the amplitude will follow a Rayleigh distribution, the intensity ($I = A^2$) an Exponential distribution, the log intensity a Fischer-Tippett distribution, and the multi-looked intensity will follow a Gamma distribution [3]. Since the resolution cell for a marine radar is much larger than the size of a capillary wave and the scatter return from capillaries can be considered random, the backscatter due to capillary waves can be assumed to follow the central limit theorem. This is confirmed by the fact that the distribution of capillary waves alone follow the Gaussian distribution as explained in chapter 2.4.2 [6]. If the number of individual scatterers N is not large enough, the CLT is not satisfied and other models must be used that are more suited to describe the *speckle*. This happens if the resolution to the sensor is very high, and/or the wavelength of the signal is large relative to the resolution cell. This will also be the case if the surface is very rough relative to the wavelength, for example with gravity waves of significant size [3].

2.4.4 The Product Model

To find a statistical model describing the clutter in rough sea states, as in figure 4 d), the product model can be used. This model is extensively used in the synthetic aperture radar (SAR) commu-

nity [3]. The product model separates the intensity into a part for the clutter σ and an uncorrelated multiplicative part n for the *speckle*, as given in equation 28.

$$I = \sigma n \tag{28}$$

Using Bayesian statistics the probability distribution of the intensity is given by:

$$P(I) = \int_0^\infty P_I(I|\sigma) P_\sigma(\sigma) d\sigma \tag{29}$$

Here $P_I(I|\sigma)$ is the correlated speckle component and $P_\sigma(\sigma)$ is the fluctuation of the clutter component (σ) which is the *texture*.

If the fluctuation of the clutter $P_\sigma(\sigma)$ is modelled by the *Gamma distribution*, the intensity can be modelled using the *K-distribution*, which is a three parameter distribution of the multiple of two *gamma distributions*. The requirement is that the speckle can be described using a gamma distribution [3]. It has been shown in [14] that *sea clutter* can be modelled using the *K-distribution*. We will not be using the *K-distribution* in this thesis, but by showing that the *Gamma distribution* can be used to model sea clutter at low sea states when $P_\sigma(\sigma)$ is approximately constant, this thesis might be a forerunner for future projects to test the K-distribution on marine radars.

2.5 Incidence Angle

As the distance from the transmitted beam to a scatterer increases the incidence angle to the scatterer is getting higher. This is visualized in figure 5. In the marine radar community depression angle is often used to describe the angle between the transmitted pulse to the horizon [11]. The backscatter will contain more of the specular part of the scattered microwave at high incidence angles and low depression angles, such that the general brightness of the sea clutter will be higher closer to the radar than further away. Water has the property that it is very specular and will act on a microwave almost like a mirror [11].

2.6 Gain control methods

The received signal strength in a radar has a very large dynamic range, and a strong signal can be a multiple of more than 100 dB to a weak signal [2]. There are several reasons for this variation in signal strength. One reason is the attenuation of $1/r^4$ due to increasing range as shown in 2.1 with the radar equation. Another reason is that different targets reflect differently and have different

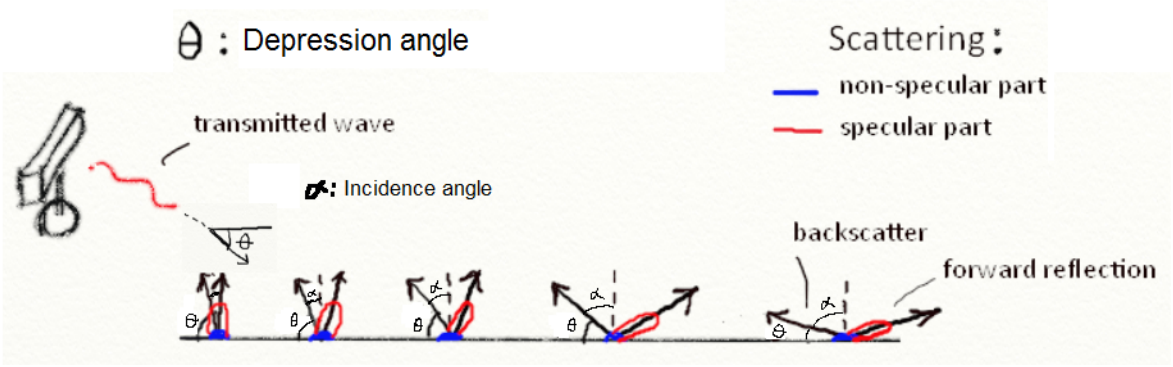

Figure 5: *Showing the amount of backscatter versus the amount of forward reflection for scatterers with increasing range and decreasing depression angle (increasing incidence angle).*

effective radar cross sections (RCS). To counter the difference in signal strength without either saturating the receiver or loosing potential targets, different gain control methods are implemented in the radar [2].

2.6.1 Sensitive Time Control (STC)

To counter the effect of the $1/r^4$ signal attenuation, sensitive time control or also called swept time constant is used. The STC adjust the gain very low at the time of transmission and then at an increasing rate of r^4 [2]. With STC the radar is thus able to receive signals from close range without being saturated, and is sensitive enough to be able to detect signals at long range. See figure 6 a).

Anti-clutter sea

Since the illuminated area depends on the beamwidth of the antenna and increase with range as shown in figure 6 b), the sea clutter is proportional to $r \times \sigma$ when we are assuming flat earth and that the range increment Δr stays the same, and σ is the radar cross section for the current sea state and r is the range [2]. If the radar cross section were constant with respect to range the total attenuation would thus be $1/r^3$ and not $1/r^4$ [2]. Although, as explained in chapter 2.4.4 and 2.5 the radar cross section of the sea is varying, and the true attenuation will therefore be somewhere between the two. Anti-clutter sea is manually adjusted on the radar by the operator and suppress the sea-clutter especially at close range to the radar. In reality it is reducing the effect of the STC to have a rate closer to r^3 dependent on how high the anti-clutter sea is adjusted [2]. To a certain range the maximum gain will be achieved and the anti-clutter sea will have no effect [2]. The details of the STC and the anti-clutter sea is seldom revealed by the radar designer and it might very well contain an algorithm that tries to estimate the current sea state and then adjust the STC accordingly [6].

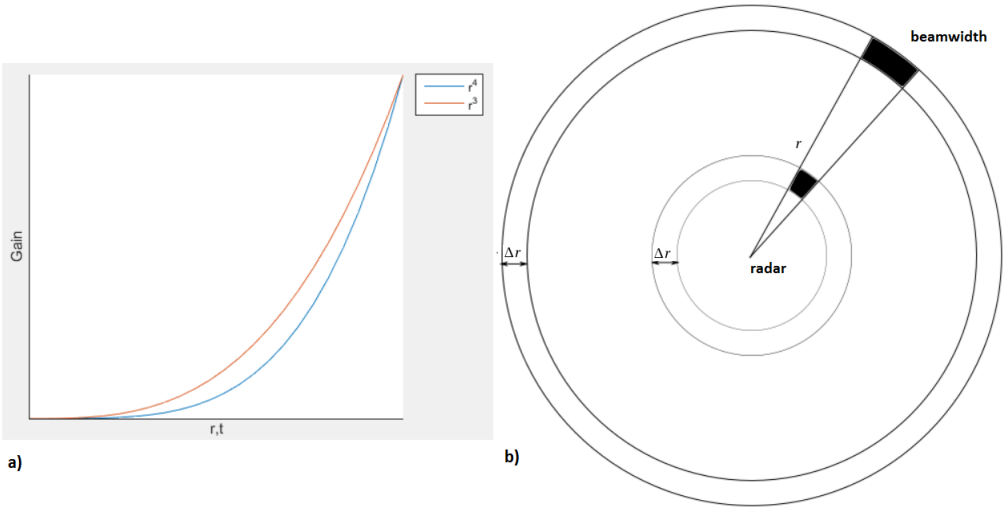

Figure 6: *a) Level of gain following a function (of time) r^4 for STC and r^3 for an anti-clutter sea (extreme) b)The azimuth resolution decrease with increasing range and the illuminated area (black) will therefore increase as the range (r) is increasing. The two cells shown have both the same range increment (Δr)*

2.6.2 The logarithmic amplifier

To be able to both receive strong and weak signals, with a difference in signal strength as much as 100 dB, many radars are equipped with a logarithmic amplifier [2, 6]. The logarithmic amplifier uses special limiting amplifiers such that the signal is separated in 10 dB increments as shown in figure 12. The first amplifier saturates at 10 dB, and the next saturates to signals higher than 20 dB, and so forth. It continuous like this until the last amplifier with the desired maximum saturation point is reached. Here only very strong signals are received [2]. In this way both very weak signals and very strong signals are preserved. Exactly how many amplifiers that are used and where they saturate depends on the radar and if sensitive time control (STC) is used prior to or after the logarithmic amplification [2].

2.7 Detection Algorithms

A detection algorithm that is widely used on marine radars and also on SAR images [15, 6, 1], is the *Constant False Alarm Rate* (CFAR) algorithm. In general, the algorithm will estimate statistical parameters such as the mean (μ) or the variance (σ) of a chosen probability density function (PDF) for cells surrounding a particular cell (or group of cells) under evaluation. This cell (or cells) is called the target cell(s), and the surrounding cells are called the *background* cells. A threshold based on the estimated parameters is used for detection. This is the reason for the naming of the algorithm, because the false alarm rate will stay constant. See figure 7 for an example of a *two-parameter* CFAR (μ,σ) which uses a Gaussian PDF to describe the background statistics and t is a

parameter decided in advance which depends on the desired false alarm rate P_{FA}.

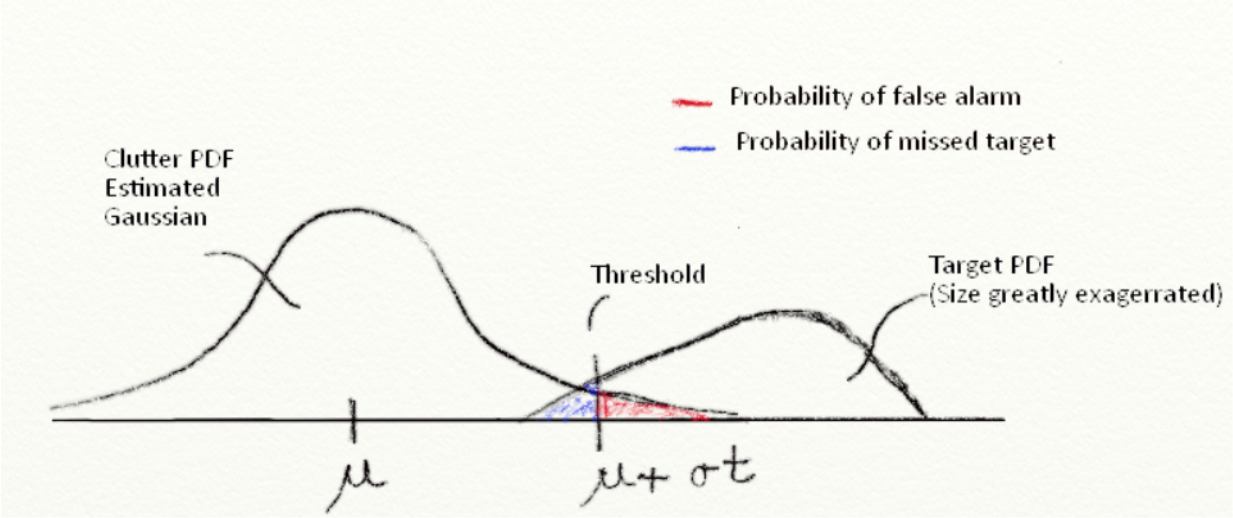

Figure 7: *Illustrating the concept that a detection threshold between two intersecting PDF's result in a probability of false alarm and a probability of missed targets. For a two-parameter CFAR the threshold might be decided by using the mean of the clutter PDF and a multiple of its standard deviation.*

Sometimes so called *guard* cells are used as a buffer between *target*- and *background* cells. This is to reduce the effect of *target* statistics mixing up with *background* statistics. Figure 8 gives an example of *target*-, *guard*-, and *background* cells for a typical marine CFAR processor, and figure 9 gives an example of these cells in 2 dimensions used on SAR images.

2.7.1 Marine CFAR algorithms

Conventionally, the CFAR algorithm used on marine radars is performed after the signal is demodulated down to baseband in the second detector. This signal is generally referred to as the video signal and is an analogue signal [6]. An overview of the circuitry for the algorithm is given in figure 8 [15]. On state-of-the-art radars the reflected radar signal might be digitized almost directly at input, so it can be assumed that the processor unit on these radars perform the detection algorithm digitally. Other radars might digitize the signal directly at output from the second detector [2]. The principle for the CFAR is nevertheless the same, and if the algorithm is as shown in figure 8, the CFAR will be performed on each radial separately and prior to the build up of the radar image [15]. Detection is therefore performed using data from only one dimension (1-D), and differ to CFAR algorithms used in SAR where a two dimensional sliding window is used [16]. There are many different CFAR algorithms, but assumed to be for competitive reasons, the radar manufacturers seldom say which one they use on their specific radar. We will mention two, the CA-CFAR

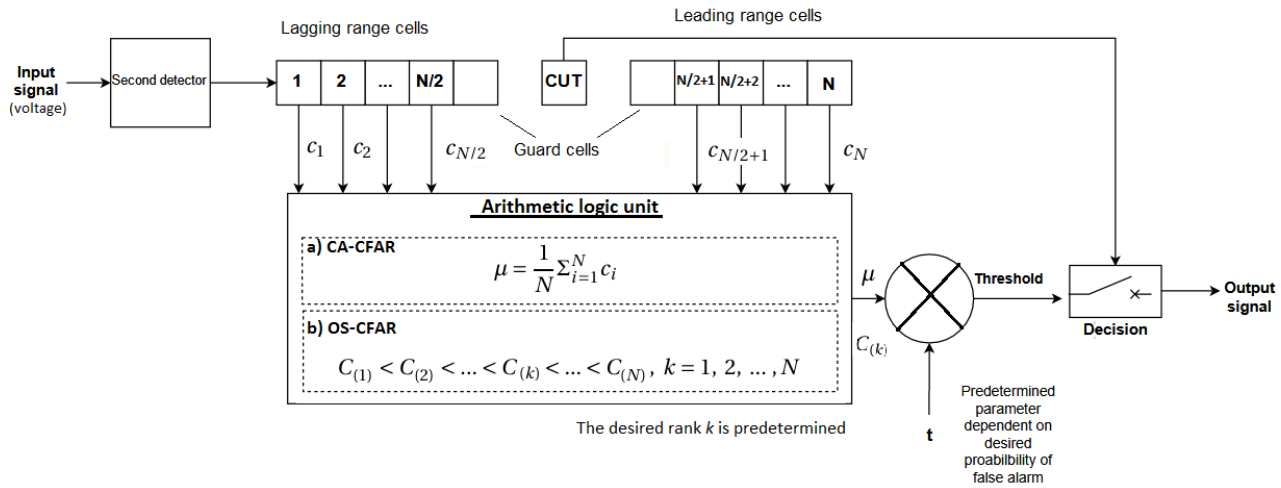

Figure 8: *A typical CFAR algorithm for a maritime radar* [15, 13, 18]

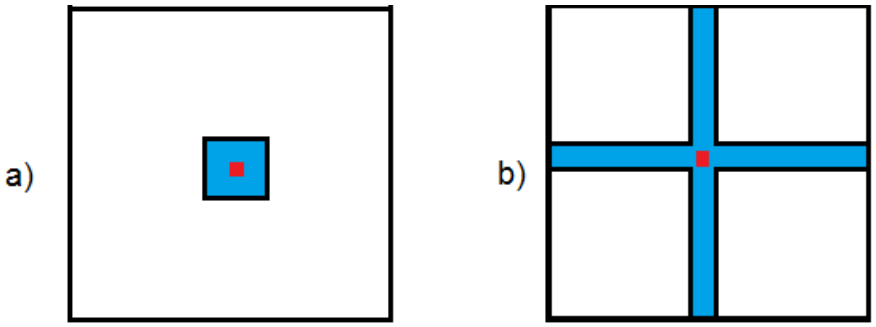

Figure 9: *2-D CFAR sliding window, where the innermost red window denotes the target window, the middle window denotes the guard window, and the outermost window denotes the background window. a) Sliding window where the guard window (blue) is surrounding the target window as a block. b) Sliding window where the guard window is formed like a cross, and there are four background sub-windows [1]*

and OS-CFAR, which seems to be the most common. The CA-CFAR is the simplest of them and probably the most usual, the OS-CFAR was proposed by *Rohling et. al.* and is proved to perform better in non-homogeneous clutter than the CA-CFAR [17].

2.7.2 CFAR algorithms used on SAR images

Target detection on SAR images is performed in two dimensions, as shown on the figure below, since the whole image is built up without any prior processing. The advantage is that background statistics are estimated from the data of two separate dimensions and not only in one dimension as in marine radars, and will therefore probably result in a more accurate estimate. The CFAR window is either chosen with guard windows surrounding the target pixels as in figure 9 a) or as

shown in figure 9 b) [1]. In the sections below we will explain the basics of what we believe is the most common CFAR algorithms used in marine radars. We will also explain the basics of the TS-CFAR algorithm which we regard as one of the state-of-the-art CFAR algorithms proposed by Tao et al. [1], and which will be tested on marine radar images in this thesis.

2.7.3 CA-CFAR

The cell averaging (CA) CFAR is the simplest of the CFAR algorithms and probably the most common. The average (μ) of the cells in the background window is calculated as shown in figure 8, and the detection threshold is decided by multiplying μ by a predetermined parameter t. If c is the cell under test (CUT), c is classified as a target if:

$$c_{cut} > \mu t \tag{30}$$

The mean μ is either linear or logarithmic (dB) depending on the IF-amplifier, and the second detector in figure 8 can either be a linear- or square law detector [11]. It is common to use guard cells around the target cell(s) for the CA-CFAR because nearby cells are often correlated with the target cell(s) which means that using them will result in the value of μ being too high and not representative for the background statistics. Other variants of the CA-CFAR is the *greatest of*- (GO) or *smallest of*-(SO) CA-CFAR, where the mean parameter μ with greatest or smallest value is selected from two or more subwindows [1, 15].

2.7.4 OS-CFAR

The *order statistic* (OS) CFAR is a non-parametric CFAR algorithm which was proposed by Rohling et al. [17, 13]. The algorithm is proved to perform better than the CA-CFAR in non-homogeneous clutter and also perform better than the CA-CFAR in multiple target situations [17]. The cells in the background window is sorted by increasing signal strength (rank), and the k'th cell is chosen as the mean for the underlying PDF for the algorithm. It is a technique adopted from image processing [17], and k can for example be chosen to represent the median, minimum or for example the maximum. Choosing $k = \frac{3N}{4}$ has been suggested to give good results [17]. The PDF of the chosen k can be derived from using the following equation [17, 1]

$$f_{C_k}(c) = k \binom{N}{k} [1 - F_C(c)]^{N-k} [F_C(c)]^{k-1} \, f_C(c) \tag{31}$$

If c is the cell under test, c is classified as a target if:

$$c_{cut} > C_{(k)} t \tag{32}$$

Where $C_{(k)}$ is the mean value calculated for the estimated PDF of the underlying model, for the k'th rank, derived from equation 32, and t is a predetermined parameter dependent on the desired P_{FA} It was shown in [17] that guard cells will not be necessary for the OS-CFAR.

2.7.5 TS-CFAR

The *truncated statistics* (TS) CFAR proposed by *Tao et al.* is a detection algorithm that outperforms both the CA-CFAR and the OS-CFAR in multiple target situations [1]. It was shown in [1] that it atleast performs on par with the *iterative censoring* (IC) CFAR, but is computational more efficient. The IC-CFAR was proposed by *Cui et al.* and uses an outlier map that is updated iteratively. This map is used to remove outliers from the data to estimate a more accurate background PDF [19]. IC-CFAR can be combined with other algorithms resulting in for instance in ICCA-CFAR or ICOS-CFAR, if combined with CA- and OS-CFAR respectively [1]. The TS-CFAR uses a truncated version of the background window to remove outliers, and uses an underlying truncated PDF for the threshold decision. Targets can be considered outliers and can usually be removed from the clutter statistics because of their high brightness. If the hypothesized PDF for the clutter is $f_X(x)$, for a random variable X, the truncated PDF is $f_X(x|X \leq t)$ as shown in the equation below [1].

$$f_X(x|X \leq t) = \begin{cases} \frac{f_X(x)}{F_X(t)}, & \text{if } x \leq t \\ 0, & \text{otherwise} \end{cases} \tag{33}$$

Here x is the value of a cell in the background window, t is the predetermined truncation level, and $F_X(t)$ is the normalization constant and CDF at truncation. By calculating the truncated version of the hypothesized clutter PDF, which is the correct PDF for truncated data, the CFAR will be able to model the clutter more accurately and therefore improve detection for situation where outliers are present [1]. Since outliers are removed from data, it has been shown that the TS-CFAR algorithm does not need guard cells [1].

Truncated Weibull PDF

To be able to use the TS-CFAR in Weibull distributed clutter, the truncated Weibull has to be found. By plugging the Weibull PDF and CDF, shown in appendix A and B respectively, in equation 33 we get the following truncated PDF for Weibull clutter:

$$f_X(x|X \leq t) = \frac{\frac{k}{\lambda}\left(\frac{x}{\lambda}\right)^{k-1} exp\left(-\frac{x}{\lambda}\right)^k}{1 - exp\left(-\frac{t}{\lambda}\right)^k} \tag{34}$$

where λ is the scale parameter, k is the shape parameter, and $x \leq t$

Truncated Gamma PDF

By plugging in the Gamma PDF and CDF which are also given in the appendix, we get the following truncated version of the probability density distribution [1]:

$$f_X(x|X \leq t) = \left(\frac{L}{\mu}\right)^L \frac{x^{L-1}\exp\left(\frac{-xL}{\mu}\right)}{\gamma(L, tL/\mu)} \tag{35}$$

As also explained in appendix B, the Gamma distribution that is frequently used in the SAR community is the distribution in terms of the parameters L and μ, where L is the equivalent numbers of looks for a multi-looked radar image. The function $\gamma(a,b) = \int_0^b y^{a-1}e^{-y}dy$ is the incomplete gamma function. The truncated version of the Gamma distribution in terms of the shape parameter k and the scale parameter θ is as follows:

$$f_X(x|X \leq t) = \frac{1}{\gamma(k, t/\theta)} \frac{x^{k-1}}{\theta^k} \exp\left(-\frac{x}{\theta}\right) \tag{36}$$

2.8 Maximum Likelihood Estimator

The maximum likelihood estimator is an estimator used to estimate the parameters of a probability density function [20]. It is based on the definition of likelihood which is that the estimation of the value of the true parameter is the joint probability of that particular parameter for N samples. If the samples are independent and identically distributed (i.i.d.) the maximum likelihood is given by the function below:

$$\mathscr{L}(p|x) = f_X(x_1 < X, x_2 < X, ..., x_N < X|p) = \prod_{i=1}^{N} f_X(x_i|p) \tag{37}$$

Where p is the parameter which we want to estimate, and $x = x_1, x_2, ...x_N$ is the N samples. For a radar image, each pixel can be considered the sum of many individual scatters, such that each pixel can be considered an individual sample. As shown in equation 37 the assumption that each pixel is i.i.d. has been made in order to justify the use of the maximum likelihood estimator, because only when this is true is the joint probability the product of the sample PDFs [12]. To maximize the likelihood, we try to find out where the derivative of $\mathscr{L}$ is zero. This is in general a complicated equation unless we take the logarithm of the likelihood which can be done because the logarithm is a function that increase monotonically. The maximum log-likelihood estimator for a parameter p is thus [1]:

$$\hat{p} \subseteq \text{argmax}\left\{\log \mathscr{L}(p|x)\right\} \tag{38}$$

The maximum likelihood estimators for the parameters of the PDFs used in this thesis is listed below.

MLE for the Weibull distribution

The log-likelihood function for the Weibull distribution is:

$$\ell(\lambda, k|x) = N\log k - Nk\log\lambda - \sum_{i=1}^{N}\left(\frac{x_i}{\lambda}\right)^k + (k-1)\sum_{i=1}^{N} log\, x_i \tag{39}$$

By using equation 38 with the restraint that $k > 0$ and $\lambda > 0$, and by solving this optimization problem, we get the following numerical equations for λ and k respectively.

$$\hat{\lambda} = \left(\frac{1}{N}\sum_{i=1}^{N} x_i^{\hat{k}}\right)^{-\hat{k}} \tag{40}$$

$$\hat{k} = \left[\frac{\sum_{i=1}^{N} x_i^{\hat{k}}\log(x_i)}{\sum_{i=1}^{N} x_i^{\hat{k}}} - \sum_{i=1}^{N}\log(x_i)\right]^{-1} \tag{41}$$

Equation 41 and can only be solved numerically. In a similar way the parameters for the Gamma and the truncated Gamma is also found, using the log-likelihood functions below.

MLE for the Gamma distribution

The log-likelihood function for the Gamma distribution using the scale parameter θ and the shape parameter k is:

$$\ell(\theta, k|x) = N\,\theta\log k - N\log\Gamma(\theta) + (\theta-1)\sum_{i=1}^{N}\log x_i - \sum_{i=1}^{N}\frac{x_i}{\theta} \tag{42}$$

MLE for the truncated Gamma distribution

The log-likelihood function for the truncated Gamma distribution is [1]:

$$\ell(\mu, L|x) = N\,L\,\log\left(\frac{L}{\mu}\right) - N\gamma(L, tL/\mu) - \frac{NL}{\mu}\frac{1}{N}\sum_{i=1}^{N} x_i + N(L-1)\frac{1}{N}\sum_{i=1}^{N}\log(x_i) \tag{43}$$

By solving this optimization problem both μ and L can be estimated and are given by the following functions.

2.9 Chi-Square Goodness of Fit Test

The chi-square goodness of fit test, or also called the Pearson's chi-squared test, is a measure of how well observed data fit estimated data generated from a given distribution [12]. The test uses an estimation of the *Chi-square* distribution to determine the goodness of fit, as shown in the following equation. The hypothesis is that either the given distribution fits the observed data, or the data is not.

$$V = \Sigma\frac{(observed - expected)2}{expected} = \Sigma_{i=1}^{k}\frac{(Y_i - n\hat{p}_i)^2}{n\hat{p}_i} \tag{44}$$

Here Y_i is the observed value of the ith bin, $n\hat{p}_i$ is the expected value of the ith bin, and n is the number of independent trials [12]. To check the goodness of fit, the number we get, V, is compared to a *Chi-square* distribution with $k-1-d$ degrees of freedom, where k is the number of bins in the histogram for the data and d is the number of estimated parameters used to generate the data.

Chapter 3

How to extract raw data

Getting raw data from a marine radar has been proven to be much more difficult than originally anticipated during this project. For that reason, and to help future projects, we will dedicate this chapter to this particular problem. We will describe the whole process from transmitting the microwave to receiving it and getting a radar image on the monitor for a marine radar. We will do this to highlight how the system works, why it works like this, and try to use block diagrams when possible to make things clear.

3.1 Marine radar block diagram

General block diagrams for non-coherent and the coherent marine radars will be summarized in this section. Afterwards, a description of where the data should be extracted and how the data was extracted for the specific radars used during this project will follow.

3.1.1 Non-coherent pulse radar

The conventional marine radar is the non-coherent radar with a magnetron oscillator. A magnetron oscillator is built up as a thick copper cylinder with several circular cavities surrounded by a strong permanent magnet. In the middle of the cylinder is the cathode (negative charge), and the outer wall with the cavities is the anode (positive charge), see figure 10. Because of the extremely powerful magnetic field from the permanent magnet, the flow of electrons going from the cathode towards the anode bends and interact with each other randomly and will eventually enter the different cavities. The physical size of the circular cavities determines the frequency of the microwaves that are generated. One of the cavities has an opening leading to the waveguide. The microwaves exit this opening randomly and with random phase and are thus non-coherent [11].

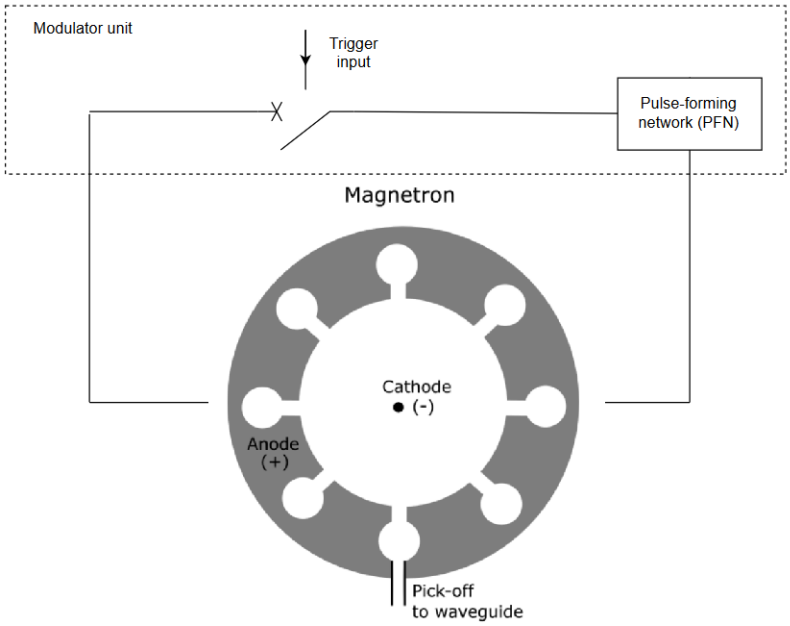

Figure 10: *Illustration of a magnetron oscillator. The flow of electrons go from the cahtode towards the anode, but the flow bends because of the strong permanent magnet surrounding the cylinder. The size of the cavities determines the frequency of the generated microwaves [11]*

Although, there exists pseudo-coherent magnetron radars where the transmitted wave is compared to a stable reference oscillator, but they are generally obsolete and will not be mentioned here [21]. In this project we have used data from the SEAHAWK polarimetric magnetron radar, the SHN-X12, and we have also figured out how to extract raw data from a FURONO radar, model FAR-3210, which also is non-coherent. Below in figure 11 is a general block diagram for a non-coherent radar [11]: The generated microwaves, in *radio frequency* (RF), from the magnetron is separated into pulses with desired pulse repetition frequency (PRF) by the *modulator unit* which controls the trigger input and the *pulse-forming network* (PFN). In conjunction with the magnetron the PFN decides the length and shape of the pulses that are transmitted [11]. The transmitted pulses enters a coupler that connects to the *duplexer* and the *mixer* [11]. The *duplexer* handles the transmitted pulses and the received pulses and make sure they are not mixed and that the receiver is not damaged by the high intensity of the transmission. The transmitted pulses from the coupler is used to calibrate the *local oscillator* (LO) to make a suitable reference wave for the *mixer*. The received echo pulses enter the *duplexer* and the *mixer* and these waveforms are mixed with the waveforms produced by the LO [11]. The output from the mixer are pulses with frequency of about 50 Mhz, the so called *intermediate frequency* (IF). A simplified explanation of what the *mixer* does is given in equation 45. Here the first term is the frequency at the input of the *mixer* (about 9.4 Ghz for a X-band radar), and the second term is the reference wave from the LO which is calibrated by the automatic frequency control (AFC) circuit. What really happens is that the signal and the reference

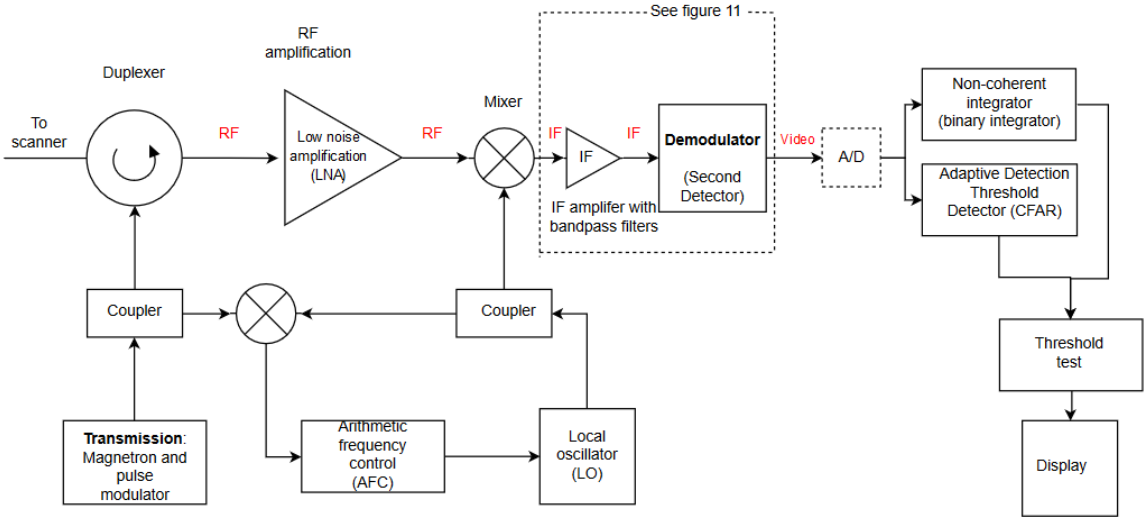

Figure 11: *General block diagram of a non-coherent magnetron radar [11, 6]*

is multiplied together which will produce sum and difference frequencies beating together. The sum frequency is discarded and the difference frequency will be about 50 Mhz [6]. The *mixer* is sometimes called the *first detector* [6].

$$9400\,Mhz\ -\ 9350\,Mhz\ =\ 50Mhz \tag{45}$$

The output from the *mixer*, now at IF, enters the IF amplifier where the signal is bandpass filtered and often logarithmically amplified [6]. Figure 12 shows an example of a logarithmic amplifier circuit with diodes that demodulates the signal to baseband (video) [6, 2]. The reason why the signal is logarithmically amplified is to preserve the dynamic range and preserve targets with low signal strength. A weak target, such as a target with low RCS as a partially submerged *growler* (small iceberg), might be just as important to detect as a vessel made of metal with a large RCS [11]. See chapter 2.6.2 for more information about the logarithmic amplifier. Regardless if the IF amplifier is logarithmic or linear, the superimposed signal (the envelope) is removed from the IF carrier by the demodulator, sometimes also called the second detector. The second detector is a diode detector that demodulates the signal down to baseband. If the voltage is low and near the origin of figure 13, the diode current is proportional to the voltage squared $I \propto V^2$ and the diode detector is a square-law detector. For such detectors the input voltage is proportional to signal power or also called intensity [6]. If the input voltage is higher and well into the linear region in figure 13 the detector is a linear demodulator and the diode current is proportional to the signal voltage $I \propto V$. Conventional radars use such linear detectors [6]. After the signal is demodulated to baseband and has become a video signal it can be displayed on a monitor [6]. Except from some pre-amplification and bandpass filtering to reduce noise, this signal is the unprocessed raw signal

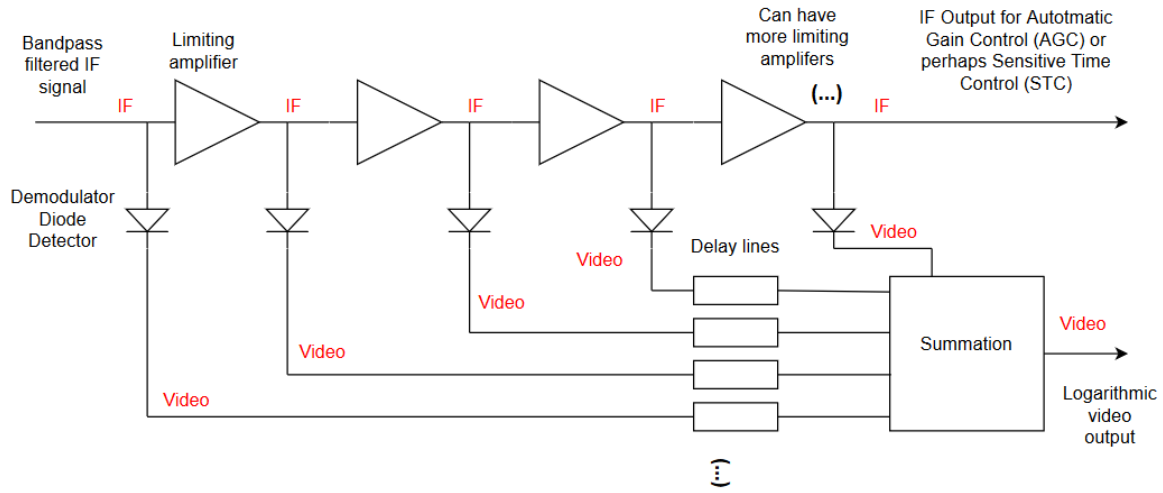

Figure 12: *Logarithmic amplifier and demodulator (diode detectors) [6]*

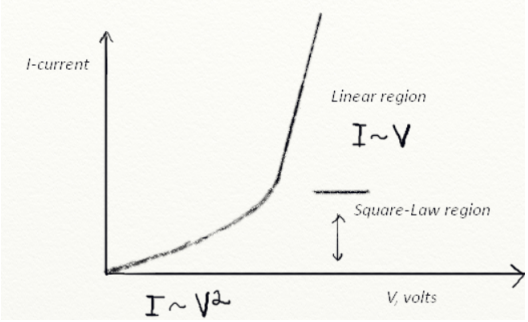

Figure 13: *Simple drawing of a diode detectors electrical characteristics. At low voltage the diode is a square-law detector and at higher voltage a linear detector [6].*

[6]. It is at this step the *raw signal* can be extracted, and it is after this step the processor unit is improving the detection capabilities of the radar with *adaptive detection threshold generators*, such as CFAR, and improving detection by the use of *binary integrators* [11]. The signal might also at this stage be digitized with a A/D converter for better processing capabilities, but the processing might also be performed on the analogue signal directly by hardware units such as the CFAR units shown in figure 8 [13, 15].

The following figure (14) shows where to extract the signal on the FURONO FAR-3210. This is a 4 V video signal, a azimuth signal from the azimuth encoder in the antenna containing 360 pulses per full rotation (one pulse per degree), a trigger signal which corresponds to the PRF of the radar, and a heading signal also from the antenna. The azimuth encoder in the antenna sends a azimuth signal every time the antenna rotates at an increment of one degree, and a heading signal every time the antenna has rotated one full rotation (one sweep)[11]. The trigger, azimuth and heading

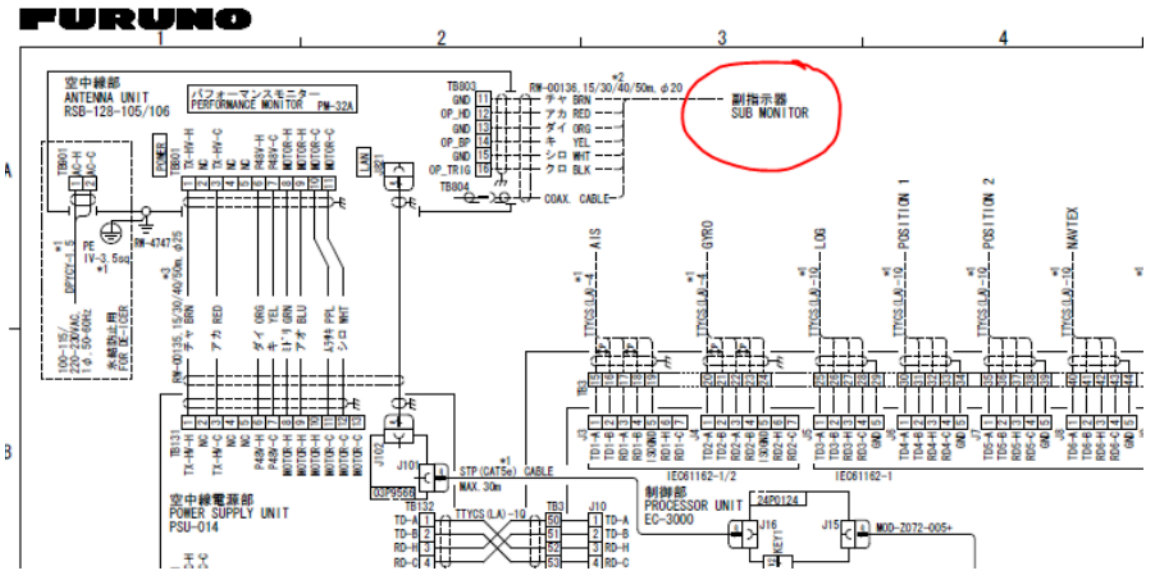

Figure 14: *Part of the manual for the Furuno FAR-3210. Marked by red is where the raw video signal can be extracted. The port is situated directly by the antenna, in the antenna box. This information was provided to us by IMES the Furono radar supplier*

signal are needed to be able to separate the signal into single pulses and to be able to separate the signal into different azimuth resolution cells.

3.1.2 Coherent pulse radar

Phase coherent marine radars with solid state oscillators have been available since the mid twentieth century. These have been frequency modulated continuous wave (FMCW) radars, and are able to separate targets at different range by continuously transmitting a beam of microwaves that increase linearly in frequency (chirp), and by using a matched filter on the reflected beam in the receiver [2]. Since these radars transmit using a large bandwidth they are able to achieve relatively good resolution by using much less power than conventional non-coherent pulse radars. The downside of FMCW radars is that they produce and receive a lot of interference, and have for these reason mainly been used on navy vessels or smaller vessels used for fishing or leisure activities [2]. We will only describe phase coherent solid state radars that are not transmitting continuous waves, but which transmit in pulses similar to the conventional magnetron radars. These have recently become affordable for the shipping industry, and the *UiT - the Arctic University of Norway* has a new model situated on the roof, a JRC radar, model JMR-9282 S-BAND , which we have been able to use for the project. These radars go under the name: «*Solid state radars*» which is a bit confusing since the FMCW radars also use solid state oscillators. The solid state radars are also using frequency modulation, but transmit in short pulses to avoid interference with other

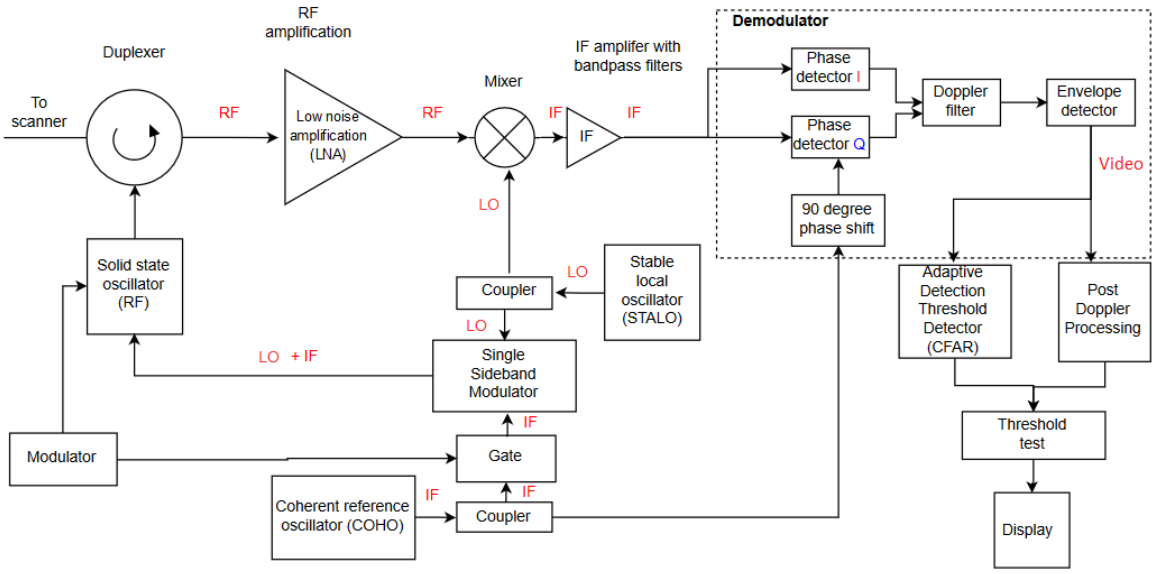

Figure 15: *A block diagram of a coherent solid state radar [11].*

vessels [2]. These radars can achieve relatively good resolution spending much less power than the non-coherent magnetron pulse radars, and since they use frequency modulation they are able use doppler filters to better be able to detect moving targets [18]. Figure 15 shows a block diagram of a typical moving target indicator (MTI) coherent pulse radar [11]:

For the JRC JMR-9282 radar we were able to extract the raw signal presumably at the stage after the envelope detector in figure 15. The envelope detector for the JMR-9282 is a linear amplifier according to the JMR-9282 manual which means that the extracted signal is proportional to the signal voltage, the amplitude. According to PRONAV, the JRC distributor in Norway, the signal processing is performed in the antenna (box underneath) and there is no straight forward way to extract the I- and Q component. This is most likely only known by JRC and is proprietary information. We were not able to get this information from JRC by contacting them directly. The raw video signal is available at the port given in figure 16 radar interface circuit (at the bridge) and is a 2 V negative signal. Additionally, a trigger signal, and a heading- and a azimuth signal (2048 per sweep) is available from the port. We extracted the video signal using the DSPNOR Multicast Asterix CAT 240 scan streamer.

3.2 The DSPNOR Scan Streamer

In this thesis we have used the DSPNOR Multicast Asterix CAT 240 scan streamer to extract and sample the raw video signal. As mentioned in the introduction to this chapter our motivation for

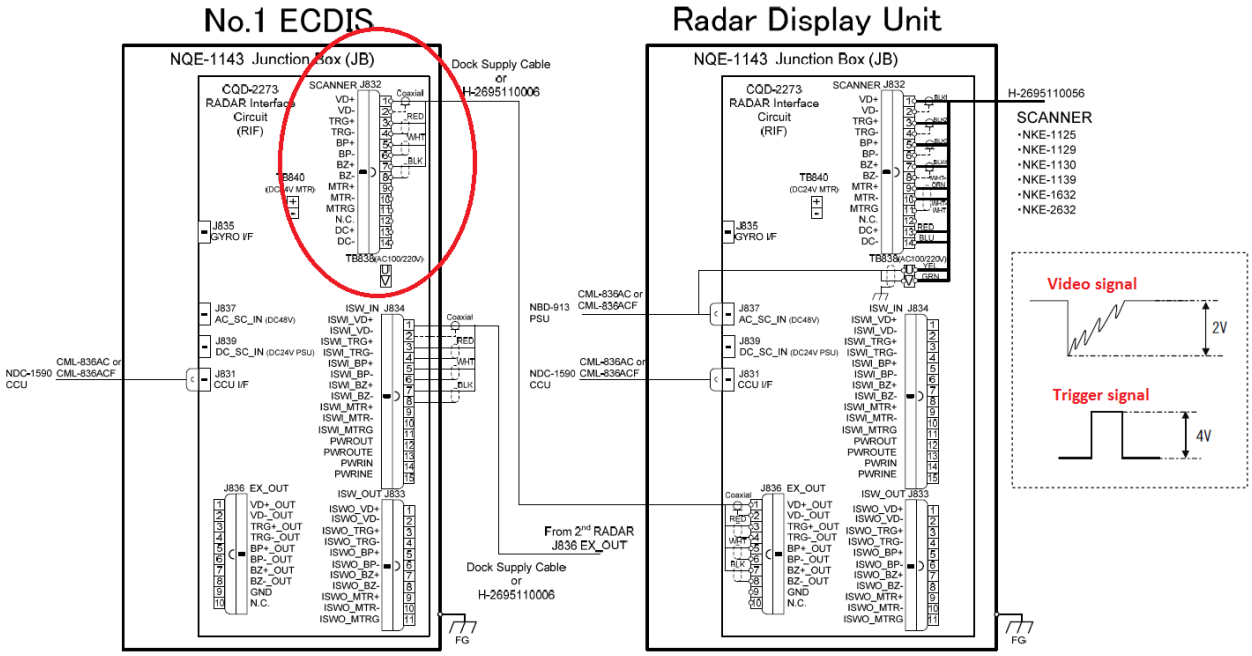

Figure 16: *Part of the technical manual for the JRC JMR-9282. Marked in red is where the raw video signal can be extracted. The video is a 2 V negative signal, the trigger takes approximately 6µ seconds from startup to video signal and is at 4 V. Both lines must be pulled up to 5 V at 1 kilo-ohm before they can be used. Information was given to us by PRONAV the JRC distributor in Norway*

writing this chapter is to help future projects facing this difficulty. This section will describe how we solved the problem using the DSPNOR scan streamer and can therefore be considered a part of the methodology of this thesis.

3.2.1 Technical Details

The DSPNOR Multicast Asterix CAT 240 board can convert any video stream to local area network (LAN) data stream, in the Asterix CAT 240 protocol. It currently supports Atlas/SAM/TVA format, Kelvin Hughes, Sperry Bridgemaster, Furuno, Consilium, and JRC, but can in practice support any radar with a analogue video output [22]. The sampling rate of the scan streamer is from 50 MHz to 120 Mhz and the maximum dynamic resolution is 14 bits. The scan streamer used in our project sampled the data at 8 bit resolution. We connected the scan streamer to the JRC JMR-9282 at the port shown in figure 16. The details of which jumper to use on the scan streamer circuit board for the specific radar was found using the technical manual provided by DSPNOR.

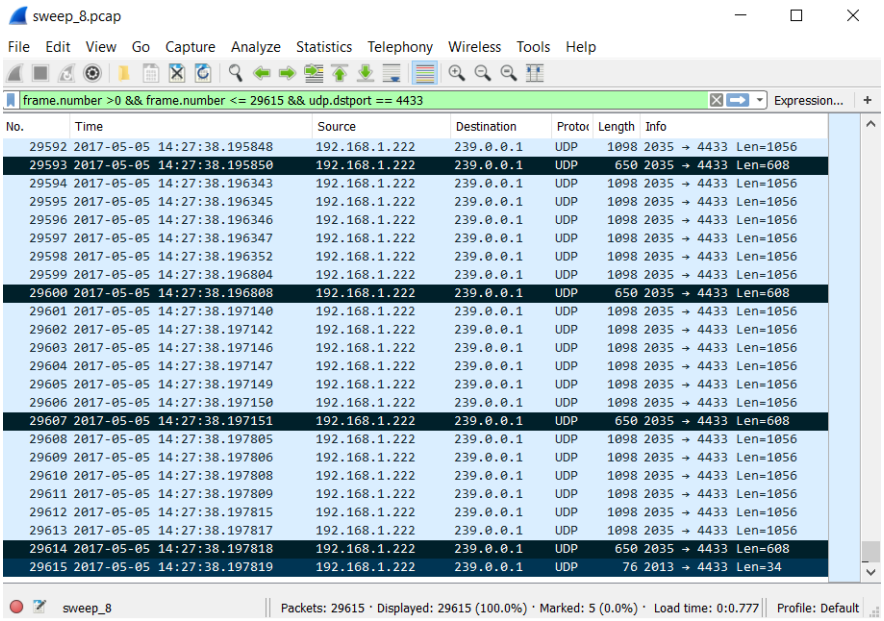

Figure 17: *Captured Ethernet frames displayed in Wireshark. The frames at Len=1056 is single pulses, the frames at Len=608 defines the end of a sector, and the frames at Len=34 defines the end of a sweep.*

3.2.2 Recording the LAN stream

The output from the DSPNOR Multicast Asterix CAT 240 scan streamer is a LAN data stream which is possible to record on a computer using a network sniffer. We have used the open source network protocol analyser, Wireshark. In Wireshark, each Ethernet frame can be analysed and sorted, see figure (17) showing captured Ethernet frames by Wireshark from the scan streamer. By analysing the frames we were able to separate the pulses in separate sweeps and save them as independent Wireshark files (*.pcap).

3.2.3 Extracting the data from the Ethernet frames

By using the buit-in function *pcaptomatlab()* we were able to open each Ethernet frame in Matlab. We used the Eurocontrol Standard Document for Surveliance Data Exchange Category 240 for Radar Video Transmission [23] available on the internet to interpret the asterix protocol. From here each frame could have been assembled together to make an image, but we had software from DSPNOR available that was able to produce a PNG image of the data for us. The purpose of this thesis was not to produce a radar image from separate pulses, but to test detection algorithms on raw data. We were able to do playback of the pcap files for the DSPNOR software by the use of the open source program Colasoft.

Chapter 4

Methodology

In this chapter we will give a thoroughly explanation of how we got our data, and how we implemented the TS-CFAR algorithm and what changes we had to do to the algorithm in order to use it on a maritime system. We have performed the algorithm both on an image (2-D) and on a radial (1-D). In order to use the TS-CFAR, the statistics for the sea clutter needed to be recognized and we had to find an appropriate model to describe it. We then had to calculate the truncated version of this model (PDF) which have been used in the algorithm.

4.1 Getting the data

The first challenge for the project was to find a way to extract raw data from the two radars we have situated on the roof of our department of the *University of Tromsø* (UiT). As explained in chapter 2, one of our radars is a non-coherent (magnetron) FURONO FAR-3210, and the other is a coherent (solid state) JRC JMR:9282. By contacting our suppliers we figured out where to extract our data which is shown in figure 14 and figure 16. Optimally, we would want to be able to extract the *quadrature-phase* (Q) and *In-phase* (I) component for the solid state radar, but it seems to be no straight forward way of doing this. We tried to look for any output in the antenna (figure 18 a)), but without any luck. By contacting JRC directly and via the supplier for JRC in Norway (PRONAV) we got a strong indication that either this is not possible, or this is confidential information that JRC do not want to share for competitive reasons. Our supplier for the scan streamer (DSPNOR) confirmed our suspicion that the signal for the JRC JMR:9282 is probably digitized directly at input to the receiver, which also complicated the issue because we would have needed equipment that interprets this information, which probably only JRC is in possession of. Our objective had to change and we had to settle with the amplitude signal extracted from the slave output, see fig-

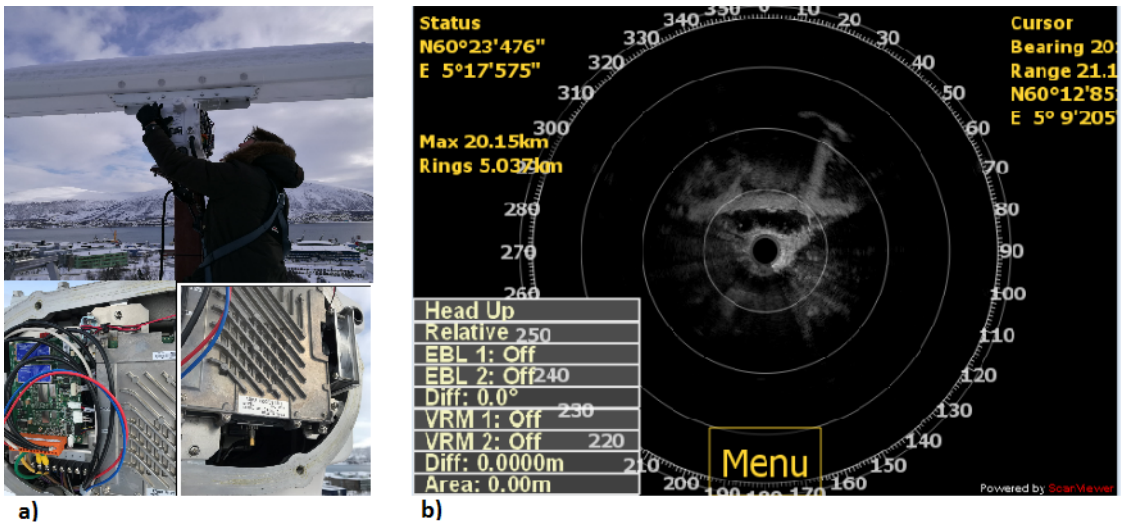

Figure 18: *a) Searching for any output for the Q- and I component in the the NKE-2632 antenna situated on the roof of the Univercity of Tromsø. b) Screenshot of the Android display for the Scan Viewer sofware while displaying real time raw data from the JRC JMR:9282*

ure 16. Our focus was now on sampling the analogue video signal, containing the *trigger signal*, the *azimuth signal*, and the actual backscatter for each beam (radial). We used an analogue oscillator and were able to visualize the un-processed radar signal, but we had no equipment available that could be used to digitize the signal. We contacted DSPNOR which were able to provide us with both the hardware and software necessary to extract the raw analogue signal, sampling it, and give us the possibility of real time display. The DSPNOR Multicast Asterix CAT 240 scan streamer was used, which converts the video stream to LAN. The details have been explained in chapter 2 and will be omitted here. Figure 18 shows the scan viewer display (DSPNOR software) when it is receiving real time raw data from the JRC JMR:9282 in Tromsø. As is evident from figure 18 and 19, our radars do not see much ocean from our position, and especially not from different incidence angles. Furthermore, strong interference from building nearby and ships in port prevent us from capturing good and representative sea clutter statistics. We had to get our data elsewhere. Sea-Hawk were kind enough to invite us to Bergen to capture data using one of their polarimetric radars, so much of the data used in this thesis is captured using the Sea-Hawk radar SHN-X12. Using the DSPNOR Multicast Asterix CAT 240 scan streamer the raw video signal (baseband) was converted to LAN, and we were able to capture (sniff) the LAN data using WIRESHARK (open source software) installed on a laptop with a windows 10 operating system. To play back the captured data we used COLASOFT which is another open source software that is able to do LAN playback. Using WIRESHARK we were able to separate the recorded data in separate sweeps. In WIRESHARK each of the relevant Ethernet frames are either a radial containing the backscatter plus some metadata (Length > 1000), a frame that defines the end of the sector (Length > 500), and a final frame

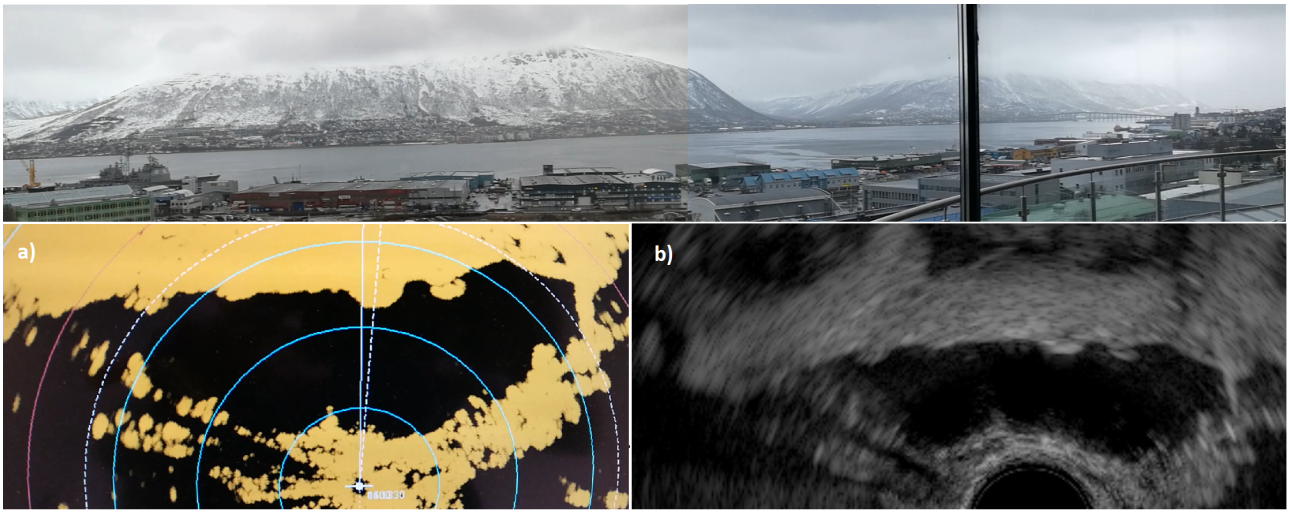

Figure 19: *a) Screenshot of the JRC JMR:9282 monitor showing processed data. b) Un-proccessed data from the scan streamer. Notice the strong interferrence from the crane to the left. There is a small vessel seen slighly to the left of the bridge in b). This target is not detected in a) since it is too close to the bridge. Both a) and b) are captured at the same time, at UTC 14:14:54*

that defines the end of the sweep (Length > 50). By knowing this we were able to separate the different recordings in separate sweeps. Each sweep could therefore be saved as an independent WIRESHARK file (*.pcap) and by using COLASOFT to play back each sweep separately and by using DSPNOR software, we were able to get a PNG image from each sweep. To get the data for the radial (1-D) algorithm we extracted the payload data for the WIRESHARK frame, one by one, and opened them in MATLAB using the built in function *pcaptomatlab()*. To interpret the metadata stored at the beginning of the frame, we used Eurocontrol Standard Document for Surveillance Data Exchange Category 240 Radar Video Transmission, which is available on the internet.

4.2 The recording process

The way we collected our data at SEAHAWK in Bergen and in Tromsø is as follows. In order to compare the TS-CFAR algorithm with present detection algorithms we had to record raw un-processed data and processed data simultaneously. The recording of the un-processed data was as previously mentioned performed using the scan streamer, and the recording of processed data was simply done by taking screen shots of the radar monitor or filming the monitor directly using a hand held camera. In Bergen at SEAHAWK, the radar monitor was uploaded to a local http server, and screen shots were captured on a computer automatically. One screen shot of the radar monitor was captured for every antenna sweep. To further confirm what was recorded, the view from our position was filmed using a GoPRO camera and a Canon Eos 100D camera on a tripod using a 70-300 mm

lens, which had the possibility of getting close up visual data of ships or other interesting targets. The timestamp on the cameras were synchronized with the watch on the radar monitors which is displayed in UTC time. Each Ethernet frame with the un-proccessed recordings also include a UTC timestamp, but notes were also written in case of erroneous data. Our direct line of sight in Bergen was about 10 kilometers and in Tromsø only about 2 kilometers, see figure 20 and figure 18.

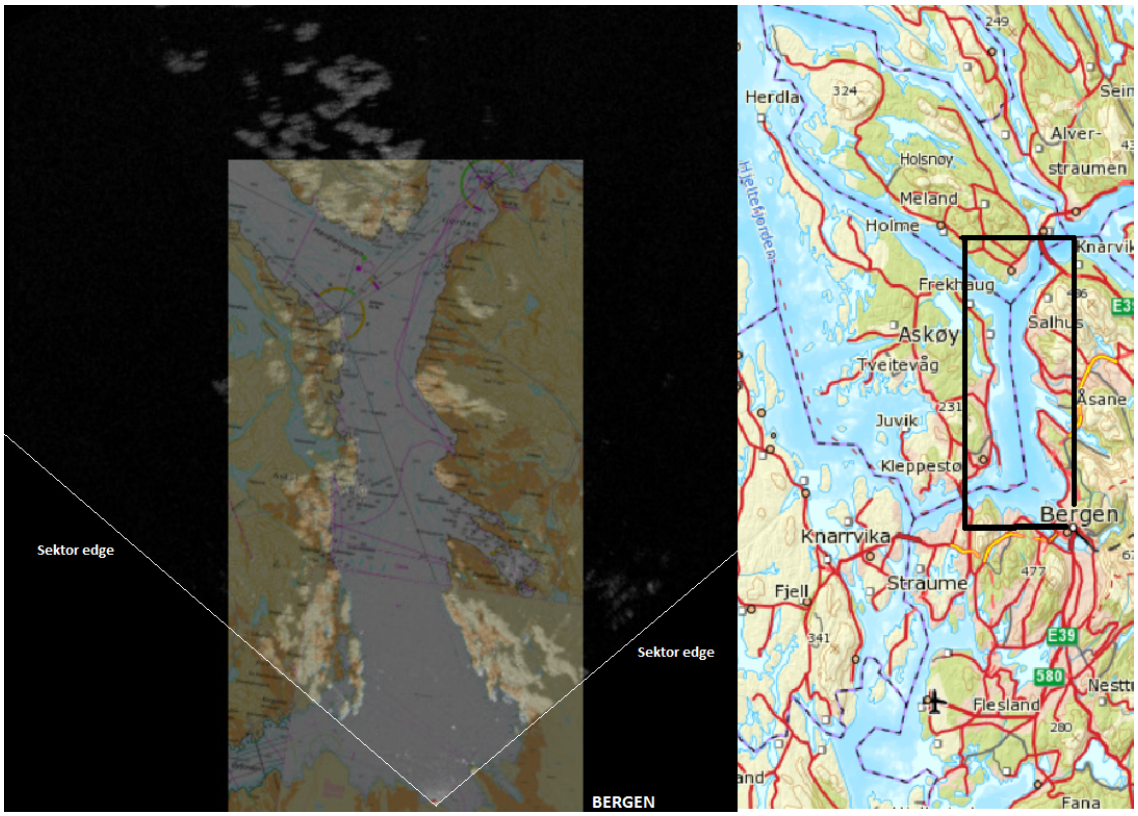

Figure 20: *A transparent nautical map layered on top of a PNG image of recorded raw data from SEAHAWK in Bergen. Both maps have been downloaded from www.norgeskart.no*

The weather in Bergen at the time of the recording was sunny and the sea was calm, but with the presence of capillary waves. All in all what is defined as sea state 2 according to the Beaufort scale . At the time of the recording in Tromsø, the weather was overcast with the possibility of local showers and the sea state was also Beaufort number 2. Look at figure 21 and figure 19 for the sea states of the recording in Bergen and Tromsø respectively.

4.3 How incidence angle change clutter statistics

We first had to test if the statistics of the sea clutter is changing for increasing incidence angle. To do this we first separated a radar image (PNG), each with increasing range and thus decreasing incidence angle. We did our best to ensure that there were only open ocean in the different sections

Figure 21: *Image of Byfjorden in Bergen at the time of the recording. Far to the left is the tip of Holsnøy just visible, which is the end of the line of sight as shown in figure 20.* The image is captured by a Canon EOS 100D with a 30-700mm lens.

and no targets present. We did this by looking at screen shots of successive scans captured from the SEAHAWK radar monitor (shown in figure 23), and looked for correlated differences that suggests a moving target. The histograms we got from four different sections, and an image displaying these sections are shown in figure 22. For further clarification, figure 20 shows a transparent section of a nautical map overlaying the radar image. This clearly shows that only the landscape in line of sight of the radar is visible, and for a radar at low grazing angles such as marine radars most of the landscape will therefore be undetected. All the steps just explained were performed using MATLAB.

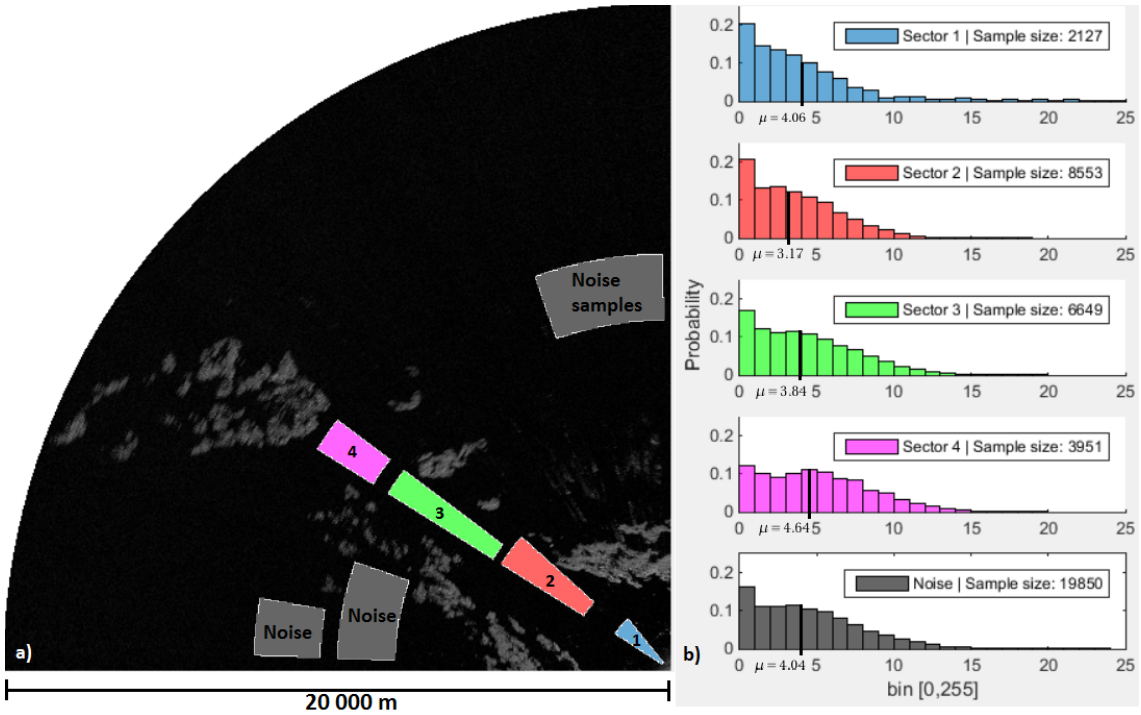

Figure 22: a) *Un-processed PNG recorded at SEAHAWK in Bergen. Four sector are extracted, sector 1 to 4 at increasing range. b) Histogram of the extracted data of the four sectors from up to 6 successive sweeps. The mean brightness μ is decreasing from sector 1 to sector 2 and then increasing.*

The overall shape of the histograms does not change much, but they all seem to contain a large amount of pixels with value zero (0 = black), which we expect is because the *gain* might have been adjusted too low during the recording for the full statistics to be captured, or the receiver was not sensitive enough. This might just as well be the purpose of the radar designer since clutter and noise is not wanted and the priority is to suppress it to improve detection. All the statistics with potentially lower values than what is shown in b) are accumulated in bin number zero because these values were too low to be captured. This is also the case for the recorded data in Tromsø by the JRC solid state radar, see figure 29. Because of side-lobe effects from nearby buildings in sector one, it is possible that this sector contains more contaminated pixels than the other sectors and might explain the longer tail. In general we would expect the mean of the brightness to decrease with respect to range and not increase as we see in 22 b). This is because the amount of backscatter received decrease with decreasing depression angle as explained in chapter 2.5. The result in 22b) might be explained as an overcompensating STC, since the gain might be adjusted to compensate for a $1/r^4$ attenuation when in reality the attenuation is less. By looking at the screen shot of the radar monitor at the time of the recording it is evident that the anti-sea clutter was off which strengthens the suspicion, see figure 23. This is because the anti-clutter sea is lowering the gain as explained in chapter 2.6.1. Although, this uncertainty lead us to investigate the possibility of the sea statistics not being fully captured, and if what we see might mostly be thermal noise. If the captured statistics is mostly noise, this would also explain the mean getting brighter for decreasing incidence angle. As the incidence angle is decreasing, less sea statistics will be captured, but the distribution of thermal noise will stay the same regardless of the range from the origin. This means that sector 3 and sector 4 are brighter because these sectors contain virtually no sea statistics and only contain thermal noise. To test this hypothesis we extracted data from a part of the radar image where we expect no real echoes, and checked if the distribution matches with the distribution of the four sections found in 22 b). As the last histogram in 22 b) shows, the noise is almost identical to the distributions we see in the two last sectors, 3 and 4. This does not mean that the recordings at SEAHAWK is useless, since the detection algorithm needs to be able to detect targets in thermal noise just as well as in sea clutter. Although, we had to get additional data in order to find an appropriate model for the sea clutter.

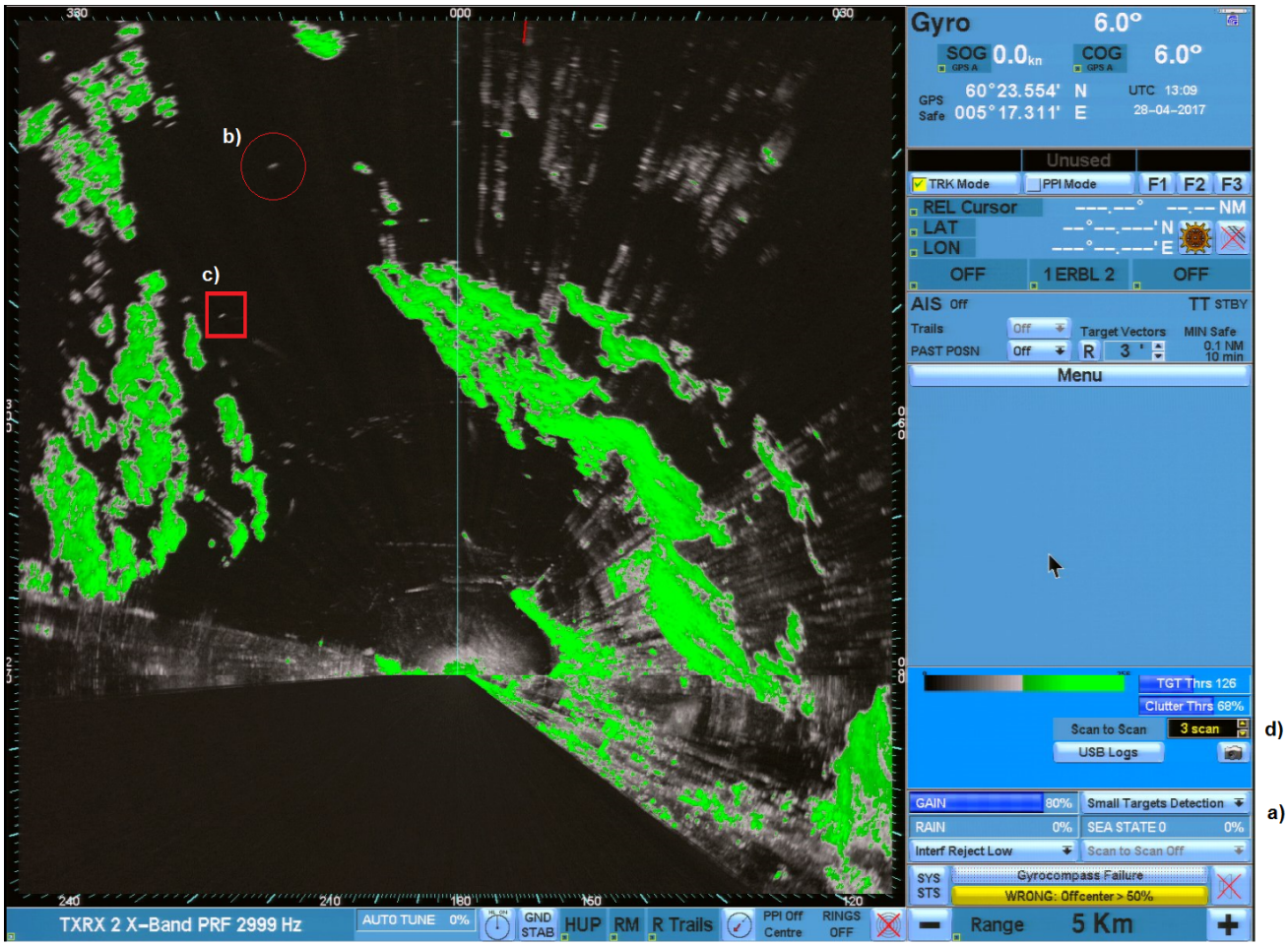

Figure 23: *SEAHAWK radar monitor at the time of the recording of the unprocessed image given in figure 22. The anti clutter sea were turned off as can be seen in lower right corner a) (Sea State 0 at 0 %). The sail boat used in some of the results is shown in b). The same sail boat is seen in c) cut in into the image from a sweep earlier in time (16 minutes). The boat in c) is smaller compared to the same boat in b) illustrating the azimuth resolution size being larger at longer range. d) The processed image is scan to scan integrated (3 scans).*

DSPNOR was very helpful and provided us with data which is presumably captured using the same Sea-Hawk radar as in figure 22, but sampled with higher spatial resolution. Now the mean brightness is getting darker with increasing range and decreasing depression angle which is as expected from sea clutter. This is shown in figure 24. Note that the outskirts of this radar image is at about 5000 meters from the radar, which means that the histogram of sector 4 in figure 24 is best compared to sector 2 in figure 22. It is evident that at long range the backscatter from the sea is so weak that the clutter distribution becomes more like the distribution of thermal noise alone. The sea clutter is always a mix of sea statistics and thermal noise [6, 11], so this result is not surprising. Nevertheless, a PDF needs to be found that is flexible enough to model the clutter PDF at any range. Furthermore, this tells us that the TS-CFAR algorithm must have windows containing data that are of similar range from the radar in order to maintain a constant false alarm rate.

The bright streaks clearly seen in the blocked sector of the radar image in figure 24 is probably radio interference from other radars or broadband devices, and explain the long tail of the noise distribution.

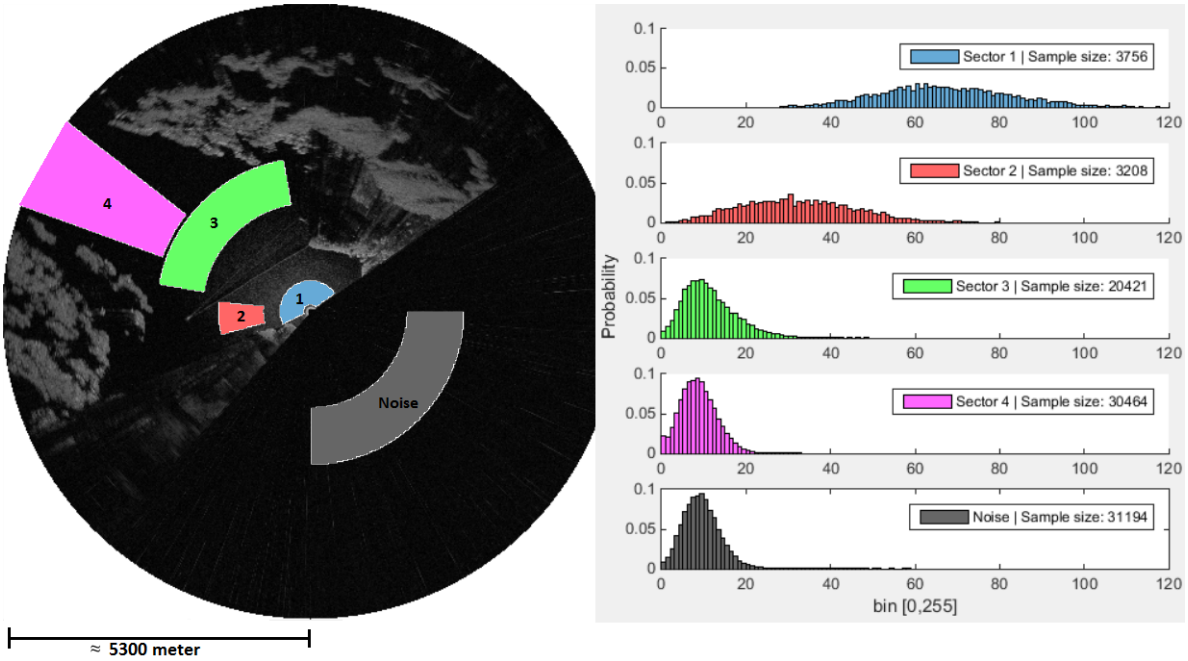

Figure 24: *a) Radar image (PNG) of un-processed data recorded at SEAHAWK in Bergen and borrowed from DSPNOR. This is the same area as in figure 20 and 22, but sampled wih higher spatial resolution. b) Histogram of the extracted data of the four sectors from this image (1 sweep).*

4.4 Workflow of the marine CFAR algorithm

First a sector map was created as shown in figure 25 b). This sector map contained filters, for all sub-sectors which the algorithm could use to extract data. The filters were images of value one for indexes contained in the sector and value zero for indexes outside the sector. This sector map is created in advance and can be designed with desired window sizes. The work flow of the algorithm is shown in figure 25 a). The cell under test (CUT) with the sliding window follow indexes defined by the sub-sector map. With this method polar window sliding is achieved. The background window is truncated for the TS-CFAR and then fed into the CFAR processor. The CFAR processor calculated the threshold by using the underlying model and predetermined truncation depth and P_{FA}. Minimizing T is an optimization problem solved in MATLAB by using the built-in function *fminsearch()*. The theory behind the CFAR processor were given in chapter 2.7.5.

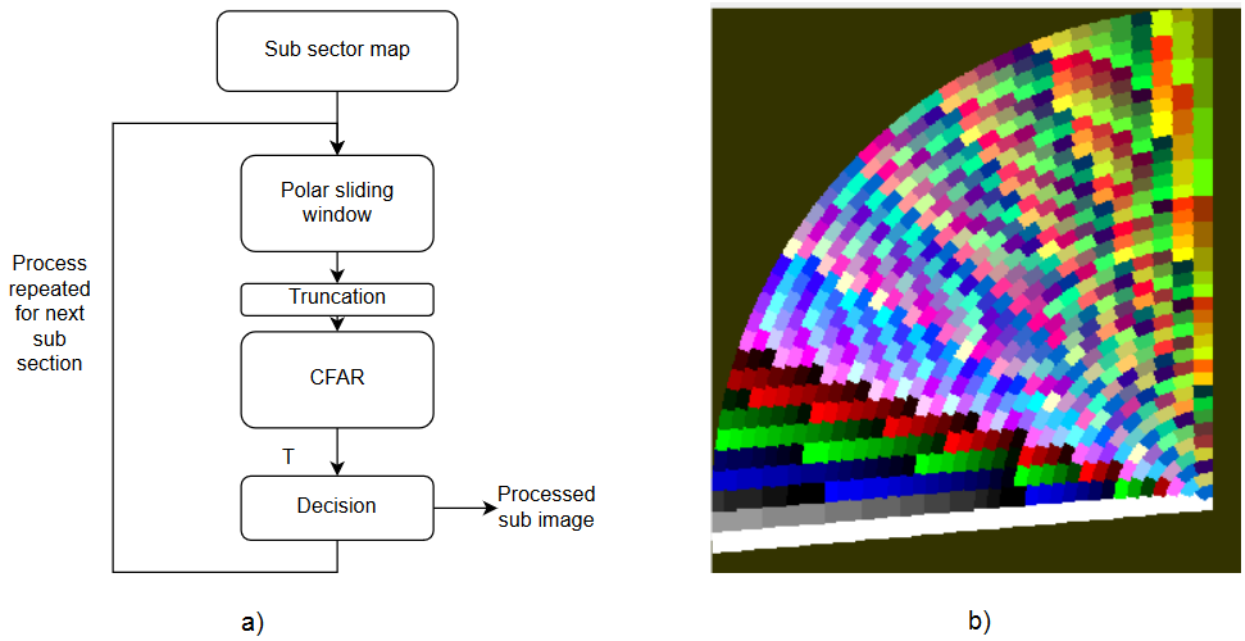

Figure 25: *a) The workflow for the marine CFAR algorithm. b) The sub-sector map. Each small sector is a filter image and the algorithm can use this filter image to extract data at a particular area, or it can extract data from all areas*

Chapter 5

Results

In this chapter the results of comparing the TS-CFAR with the CA-CFAR will be presented. We will use the TS-CFAR that models the sea clutter using the truncated Gamma model. The TS-CFAR was developed by *Tao et al.* [1] and discussed in chapter 2.7.5. Conventionally the CA-CFAR in marine radars have been using the Rayleigh or the Weibull PDF to model the sea clutter [6, 13]. To strengthen the comparison between the TS-CFAR and the CA-CFAR we have used both a CA-CFAR that is modelled using the Weibull distribution and a CA-CFAR that is modelled using the Gamma distribution. First, a model comparison will be given to justify the use of the Gamma model on marine radars. A thorough review of the sea clutter statistics is also essential in the comparison between marine radars and SAR, as the underlying model for a detection algorithm is very important for the accuracy of the detection. We have used data from the SEAHAWK radar captured in Bergen and data from the JRC JMR:9282 captured in Tromsø. Images with only one target and images with multiple targets will be used in the comparison.

5.1 Sea clutter model comparison for captured data

Sea clutter has been modelled in marine radars using the Rayleigh distribution, which is also mentioned in chapter 2.4.4 [24]. Studies have shown that for low sea states when the distribution of capillary waves is near Gaussian distributed, this model is a good fit to the data [6]. This is under the assumption that amplification in the radar receiver is linear and the voltage is thus proportional to the amplitude of the signal [6, 13]. Furthermore, studies has also shown that the Log normal distribution is a good model for high sea states because of its long tail [6, 13]. None of the models mentioned above is flexible enough to describe both low- and high sea states. For this reason, the Weibull distribution which is a two parameter PDF, was proposed by *Sekine et al.* [13]

to describe the full sea clutter statistics. The Weibull distribution equals the Rayleigh distribution when its shape parameter k equals to 2, and has a longer tail for higher $k's$ and will for that reason be somewhere between the Rayleigh and the Log normal for high sea states [6]. See appendix B for a more thorough explanation of the PDF's mentioned. In the SAR community the Gamma model is often used to model sea clutter, particularly for multi-looked intensity images, and is also a two parameter PDF [3]. If the Gamma model proves to be sufficiently good at modelling sea clutter from data captured by marine radars, algorithms developed by the SAR community might be directly used on marine radars for the benefit of the maritime community, and opposite. It is very important to find a good model for the clutter in order to improve detection of a CFAR algorithm. For these reasons, we tried to see which of the four different distributions that had the best fit for our data. We used maximum likelihood to estimate the different parameters for the Rayleigh-, Log normal-, Gamma-, and the Weibull distribution, which is simple to do in MATLAB by using the built-in functions *raylfit()*, *lognfit()*, *gamfit()* and *wblfit()* respectively. We have used the parameters calculated using a 95 % confidence interval. Figure 26 shows the result of the comparison for high resolution SEAHAWK data and figure 27 for low resolution SEAHAWK data, corresponding to figure 24 and figure 22 respectively. Figure 28 shows the result for data captured in Tromsø by the JRC solid state radar. Only the tails including the last brightness levels are included since that is the relevant part for detection using CFAR as shown in chapter 2.7.5 and figure 7. The histograms are given in decibel scale. Discarding pixels with value 0 will probably improve detection for data such as for the low resolution data captured at Sea-Hawk in Bergen, and for the low resolution data captured by the JRC radar in Tromsø . By comparing the histogram in figure 29 by the histogram in figure 28 it is evident that discarding zero value pixels improves detection. Most of the PDF's shown in figure 29 fit the data better. We also performed the *chi-squared goodness of fit* test by using the *chi2gof()* function in MATLAB which also confirms this hypothesis, and the results from this test are given in figure 30. According to the goodness to fit test and the model comparison it is the Weibull and the Gamma that fit the data best, except for sector one for the low resolution Sea-Hawk data, where the Log normal distribution fit the data best. The sector might have been to long at this range as the brightness for the clutter is changing rapidly at short range. This can be seen by comparing figure 24 by figure 22. Sector one in the low resolution image covers the same range as sector one, two and three in the high resolution image. The distribution might therefore be a mixture , which might explain the long tail. The Gamma model fit the data best for sector one and sector three, and the Weibull model fit the data best for sector two and sector four for the high resolution data according to the goodness of fit test. Although, by looking at the tail in figure 26 for sector four it is evident that the Weibull misses the brightest pixels and that actually the Rayleigh

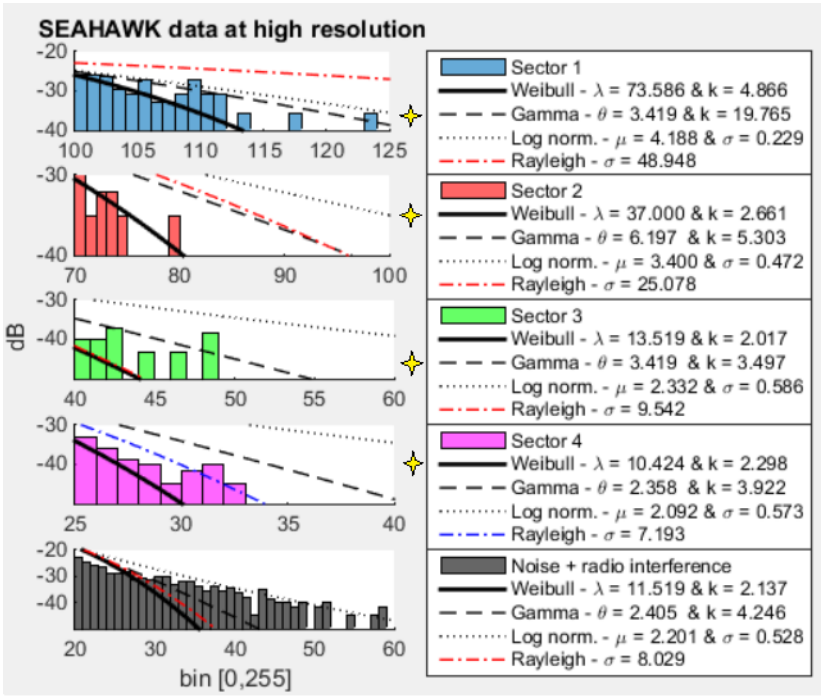

Figure 26: *Comparison of four differet PDF's to the data from the four sectors in figure 24 of the high resolution radar image captured by the SEAHAWK radar. The star denotes the goodness of fit test winner*

fit the tail better. It is fair to say that the Gamma model describes the sea clutter at low sea states sufficiently, and we can therefore go on by testing the performance of the CFAR algorithms using this distribution. As a last model comparison we extracted data from a sector containing the large wake behind the ship in figure 24. This is the closest we come to a high sea state for our data, and the waves are probably most similar to swell as was discussed in chapter 2.4.2. The sea clutter will therefore have a textural appearance which is clearly evident looking at the image. The Gamma distribution proves to be the best fit for this data which is shown in figure 31.

5.2 Algorithm performance on a single target image

We will here present the result of the comparison between the CA-CFAR and the TS-CFAR. We will test the algorithms on data captured by the Sea-Hawk radar for both low and high resolution, and on data captured by the JRC in Tromsø. We have used a window of size 33×33 for the background window for the first two experiments, and for the CA-CFAR on the first experiment we have used a guard window of size 5×5. The window size must be kept relatively small since the clutter statistics is changing with respect to range as explained in chapter 2.5. For the CA-CFAR the guard window must be large since targets might occupy several pixels on radar images captured by marine radars. For the same reason the truncation depth for the TS-CFAR must also be high, in order to make sure that absolutely all targets are removed from the background statistics. We decided to have

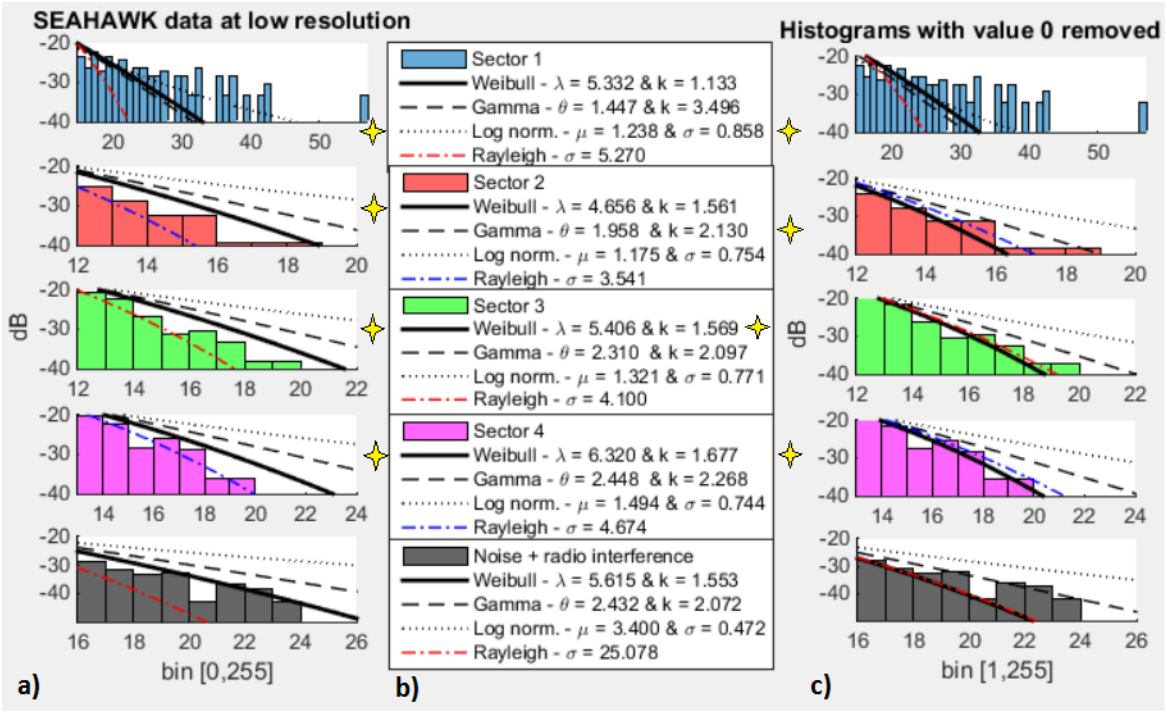

Figure 27: *Comparison of four differet PDF's to the data from the four sectors in figure 22 of the low resolution radar image captured by the SEAHAWK radar. The histograms in a) include the pixels with value 0 and for the histograms in c), pixels with value 0 are removed. The parameters in b) corresponds to the histograms in a). The star denotes the goodness of fit test winner*

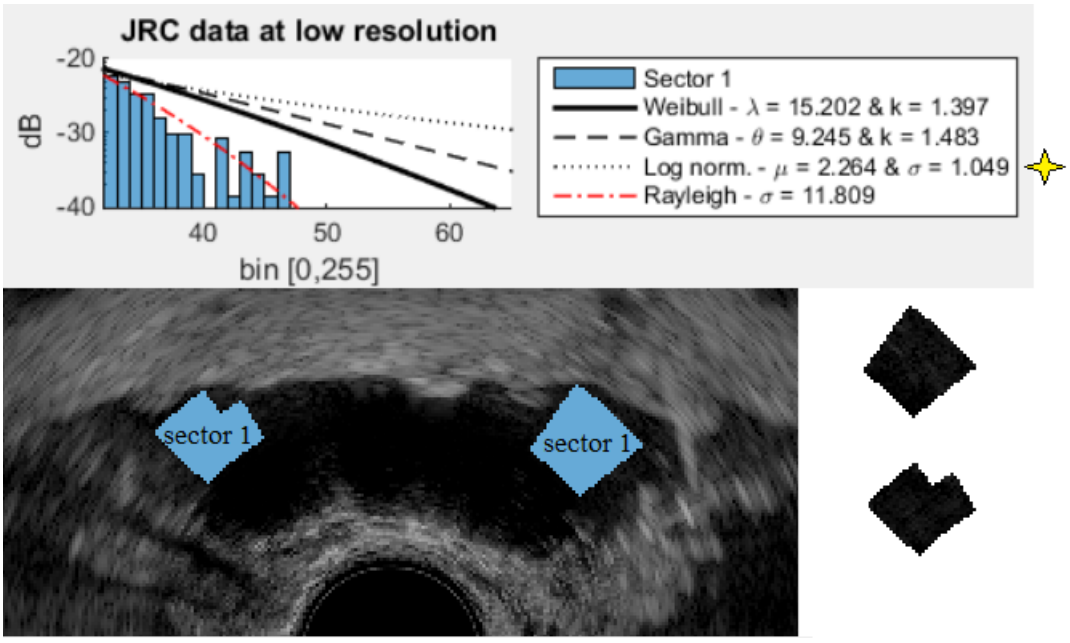

Figure 28: *Comparison of four different PDF's to captured data from the JRC solid state radar in Tromsø. Data is collected from 6 successive sweeps with a total samle space of 7008 pixels. Both sectors is at the same range and was the only areas where we could extract uncontaminated sea clutter. The darker clutter area at shorter range than the two sectors we expect is the data from the short pulse transmitted by the radar ahead of the main frequency modulated pulse. The star denotes the goodness of fit test winner*

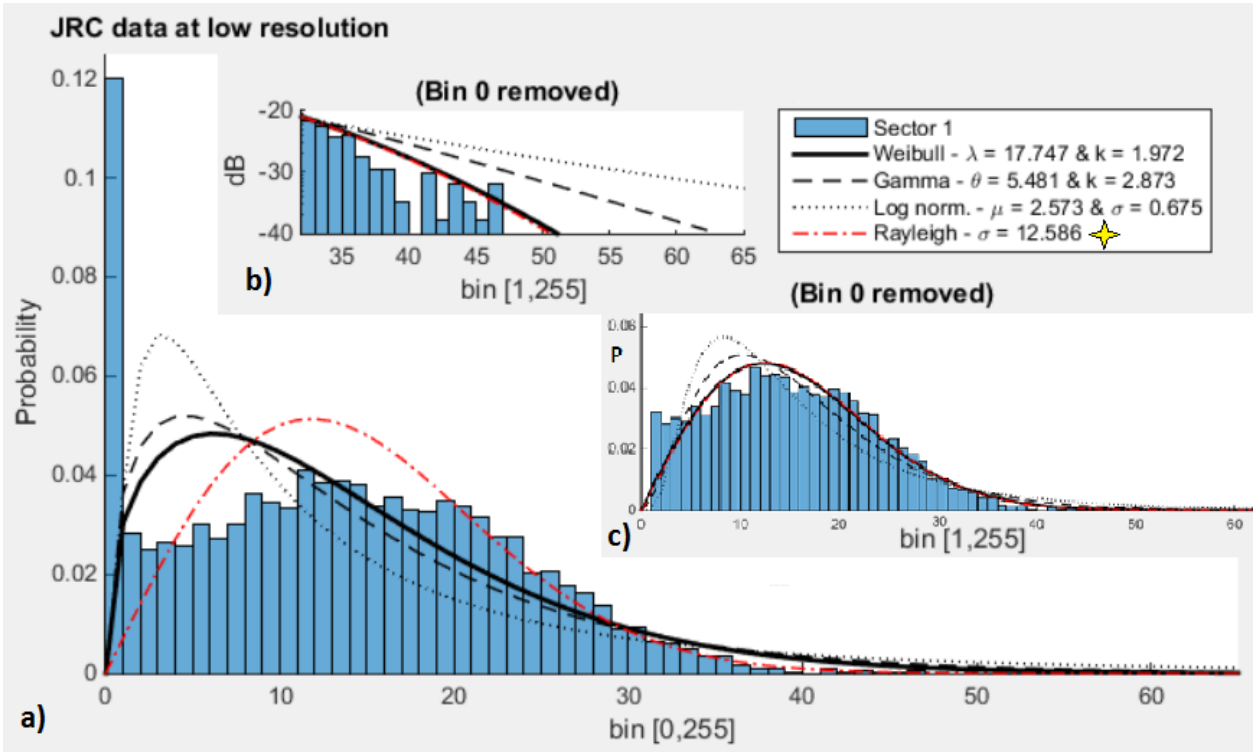

Figure 29: *a) Histogram of the extracted data from the two sectors in figure 28 of 6 successive sweeps. The data probably contain so many pixels with value 0 for the same reasons as explained in section 4.3 b) Comparison of the four PDF's when bin 0 is removed, notice that the Weibull distribution now equals the Rayleigh distribution with $k \approx 2$ which is expected at low sea states. c) Histogram with bin 0 removed. The star denotes the goodness of fit test winner.*

GOF_test_results =

'PDF'	[1]	'DSPNOR'	'SEAHAWK'	'SEAHAWK no 0'	'JRC'	'JRC no 0'
'Weibull'	[2]	[]	[]	[]	[]	[]
'Sector 1'	[3]	[6.3245e-32]	[1.0729e-41]	[2.9175e-61]	[1.1983e-139]	[5.4286e-30]
'Sector 2'	[4]	[0.2082]	[5.3121e-27]	[1.4608e-10]	[]	[]
'Sector 3'	[5]	[1.1412e-114]	[1.3354e-39]	[1.5403e-04]	[]	[]
'Sector 4'	[6]	[2.1869e-109]	[2.1953e-21]	[0.0155]	[]	[]
'Gamma'	[7]	[]	[]	[]	[]	[]
'Sector 1'	[8]	[7.7133e-06]	[1.0463e-56]	[8.4366e-52]	[1.7746e-225]	[3.0490e-89]
'Sector 2'	[9]	[2.9646e-18]	[2.2823e-67]	[1.1875e-08]	[]	[]
'Sector 3'	[10]	[2.4512e-39]	[2.4026e-42]	[8.6804e-17]	[]	[]
'Sector 4'	[11]	[0]	[2.0166e-28]	[9.2309e-13]	[]	[]
'Log normal'	[12]	[]	[]	[]	[]	[]
'Sector 1'	[13]	[2.2832e-18]	[6.5784e-04]	[5.1836e-27]	[0]	[4.7013e-223]
'Sector 2'	[14]	[7.6274e-65]	[1.0728e-230]	[1.8476e-47]	[]	[]
'Sector 3'	[15]	[3.1359e-211]	[1.4457e-89]	[1.9143e-64]	[]	[]
'Sector 4'	[16]	[0]	[9.6480e-71]	[1.1917e-48]	[]	[]
'Rayleigh'	[17]	[]	[]	[]	[]	[]
'Sector 1'	[18]	[0]	[1.4172e-291]	[1.1641e-186]	[9.5278e-259]	[2.1226e-29]
'Sector 2'	[19]	[5.0566e-64]	[2.6837e-83]	[4.9763e-13]	[]	[]
'Sector 3'	[20]	[2.2103e-115]	[4.8338e-231]	[2.3125e-06]	[]	[]
'Sector 4'	[21]	[2.4209e-321]	[3.6745e-89]	[4.8480e-07]	[]	[]

Figure 30: *Table of the goodness of fit score for the different PDF's on data extracted from the SEAHAWK radar provided to us by DSPNOR (high resolution) at the first column, and data from the SEAHAWK radar at low resolution both with and without zeros in the next columns, and then the same for the JRC radar. The boxed ones with color is the test winners for each sector.*

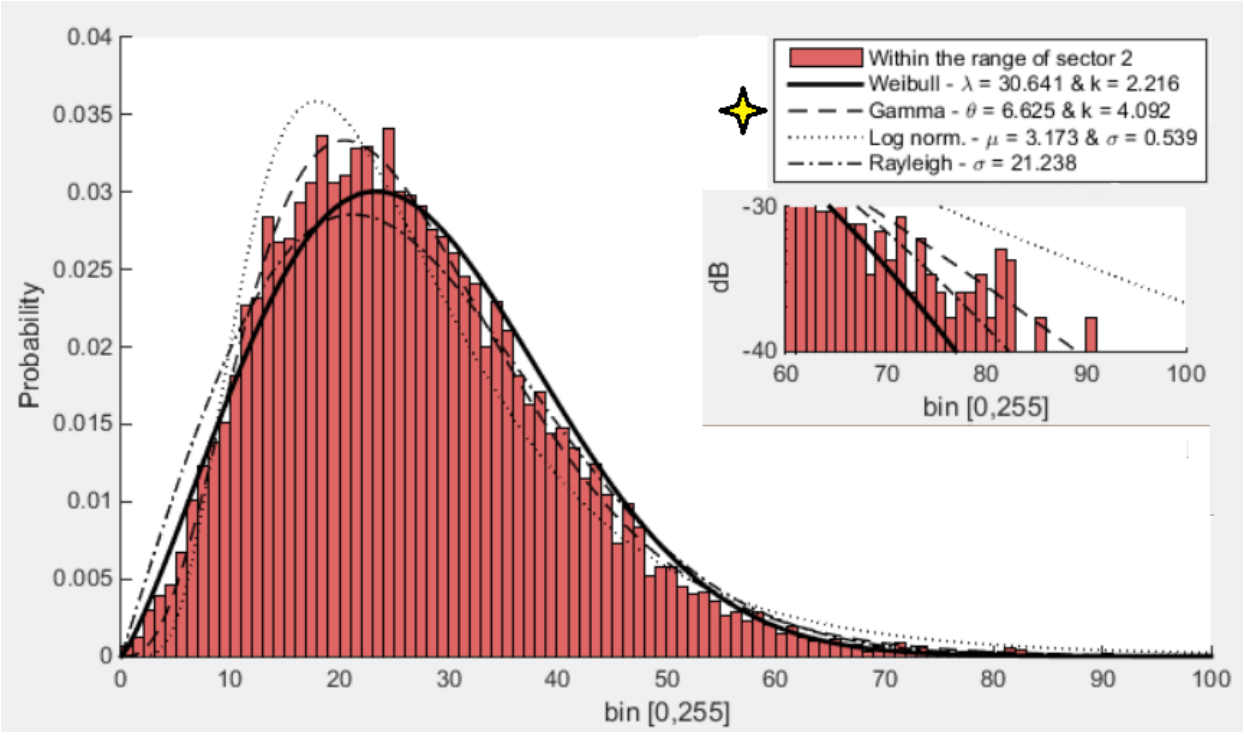

Figure 31: *Comparison of the four PDFs on data containing the ship's wake seen in figure 24. The Gamma distribution fit the data well and better than the other distributions. The goodness of fit test scores were: 1) Gamma* - 1.8×10^{-9} *2) Weibull* - 3.4×10^{-40} *3) Log normal* - 6.2×10^{-44} 4) Rayleigh - 2.8×10^{-109}

a truncation depth of 15 % for the first two experiments. This ratio we found by counting the amount of target pixels in sort of the worst case scenario, when there are very many target pixels in the background window, and finding the ratio of target pixels to the total amount of pixels in the window. We then added an extra 5 % to be sure. The truncation level is calculated by reshaping the image to a vector and sorting the pixels of the image by increasing brightness and then cut the brightest part in accordance to the truncation depth. Thus for a truncation depth of 15 %, the 85 % darkest pixels are kept and the rest is discarded. The truncation depth can also be adjusted empirically:

$$t = t_c \times x_{\max} \tag{46}$$

Where $x_{\max}$ is the brightest pixel in the image and $t_c \in [0,1]$ is a constant.

5.2.1 Experiment 1

The first experiment was performed on a polar section extracted from sector three of the high resolution Sea-Hawk radar image. An example of a background window containing many target pixels is shown in figure 32 a) and the result of truncating 15 % of the brightest pixels. The image is one of the many background windows for the TS-CFAR sliding window used on the sector shown in b).

Moreover, the performance of the different CFAR algorithms are shown, and a histogram of clutter statistics from a sliding window containing no clutter is shown in c) and d). The sliding window has a 5×5 guard window shown as a dark square in the middle, and is used for the CA-CFAR. The results are shown both for $P_{FA} = 10^{-2}$ and for $P_{FA} = 10^{-6}$. The Weibull model was compared to the Gamma model for the CA-CFAR, and it is evident that the CA-CFAR using the Weibull model detected more target pixels at $P_{FA} = 10^{-6}$. This result agrees with the estimated Weibull and Gamma distributions shown in c). Look particularly at the tail shown in decibel scale. The Gamma distribution has a longer tail, but only where there are no pixels, and as the P_{FA} is lowered the threshold will be pushed further to the right. It is safe to say that the TS-CFAR outperforms the CA-CFAR on this section, even when the truncated Gamma distribution is used and not the truncated Weibull. In other words, the TS-CFAR is best compared to the CA-CFAR that uses the Gamma model. By increasing the P_{FA} on the TS-CFAR, the wake behind the ship is also detected. This could be of interest depending on what the purpose is for the detection algorithm. If the purpose is pure ship detection and keeping the clutter and noise level at its absolute minimum, the radar designer would want to adjust the P_{FA} very low.

5.2.2 Experiment 2

Next, in figure 33, the algorithms were tested on a weak target at considerable range. It is a sail boat between sector 3 and sector 4 in figure 22, and it is about 10 km range from the radar. The sector in figure 33 is thus extracted from a low resolution radar image captured at Sea-Hawk. The pixels with value 0 were removed from the data as discussed in section 5.1. The results from using the CA-CFAR with the Gamma model is identical to the result using the TS-CFAR which is not surprising since there is only one small target present, and truncating the data will therefore have little benefit. At the outskirts of the sector the background window sees some land, as shown in c) and truncation successfully removes these pixels as shown in the lower image. The Weibull model has a better fit for the data as shown on the decibel scale in b), and also got the highest score using the goodness of fit test. For that reason, the CA-CFAR using the Weibull distribution outperforms both the TS-CFAR and the CA-CFAR which both are using the Gamma model. The truncation depth is kept at 15 %, but the guard window for the CA-CFAR is reduced in size to 3×3 since the spatial resolution is much lower, and the targets do not occupy several pixels. Furthermore, the sail boat is also detected in the processed image in figure 23 b), seen in the upper left corner.

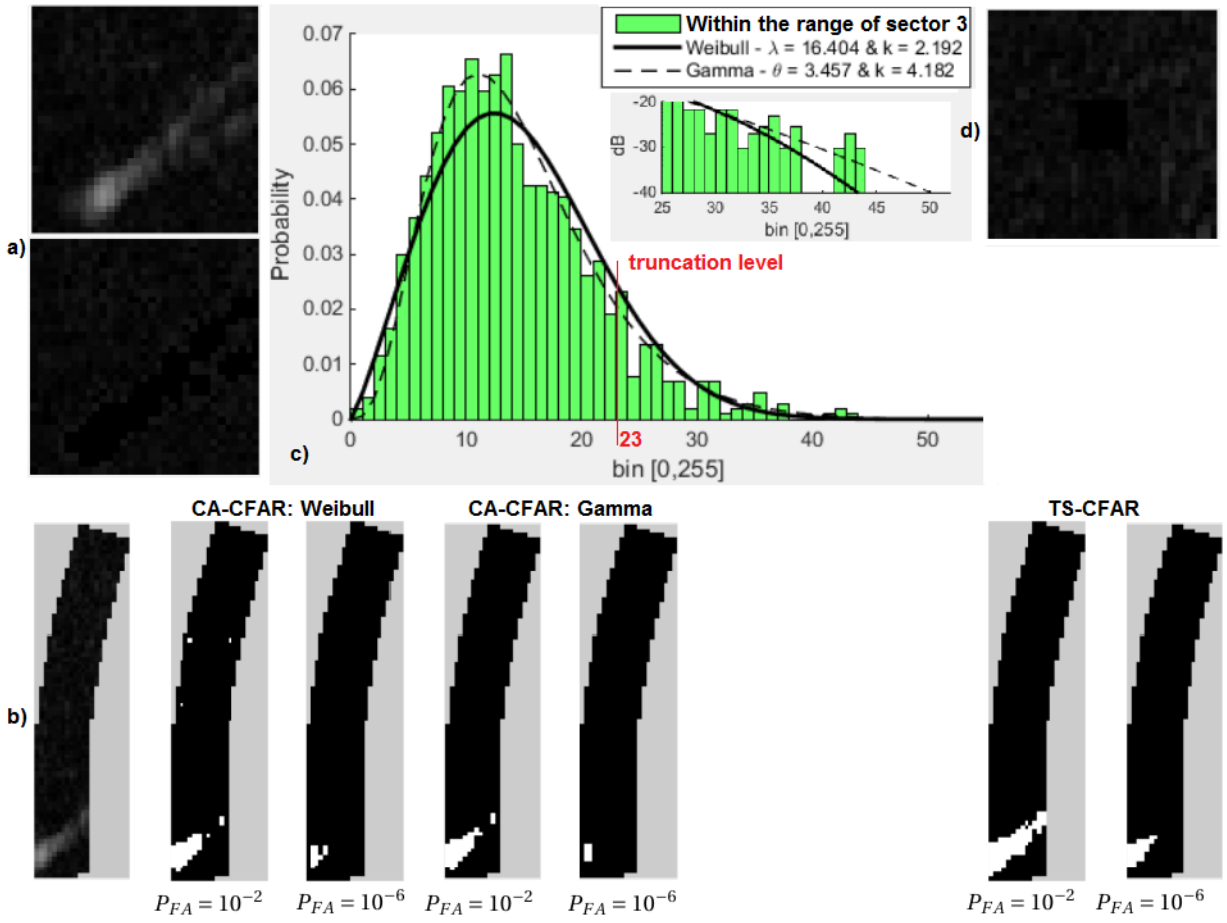

Figure 32: *Result from using CFAR on b), a selected sector containing one target. The ship is magnified in a), which is one of the* 33 × 33 *sliding windows used for the CFAR algorithm. The image just below is the same window that is truncated for the TS-CFAR alogrithm. The histogram in c) contains data extracted from one of the sliding windows containing only clutter, which is shown in d). This sliding window contains a* 5*x*5 *guard window. The ship with the wake is the same as seen in figure 24 just below sector 3.*

5.2.3 Experiment 3

Finally, the results from using the CFAR algorithms on captured data from the JRC radar in Tromsø is shown in figure 34. Since the spatial resolution of our data was very low and because of the location of our radar, very little sea clutter was captured and all the data was surrounded by land clutter. We nevertheless made an attempt for the CFAR and model comparison, on the sector shown in a). For the reason just mentioned we used a small background window for all the algorithms of only 13 × 13 pixels. We kept the guard window for the CA-CFAR at 3 × 3 pixels. Because land clutter is dominant in the image we used a very high truncation depth of 70 % for the TS-CFAR which results in a truncation level of 44. As seen in figure 34 by comparing b) and c), it is evident that the land clutter is removed from the statistics by the truncation. The pixels with value zero are removed from the data as discussed in the previous section and the histogram and model

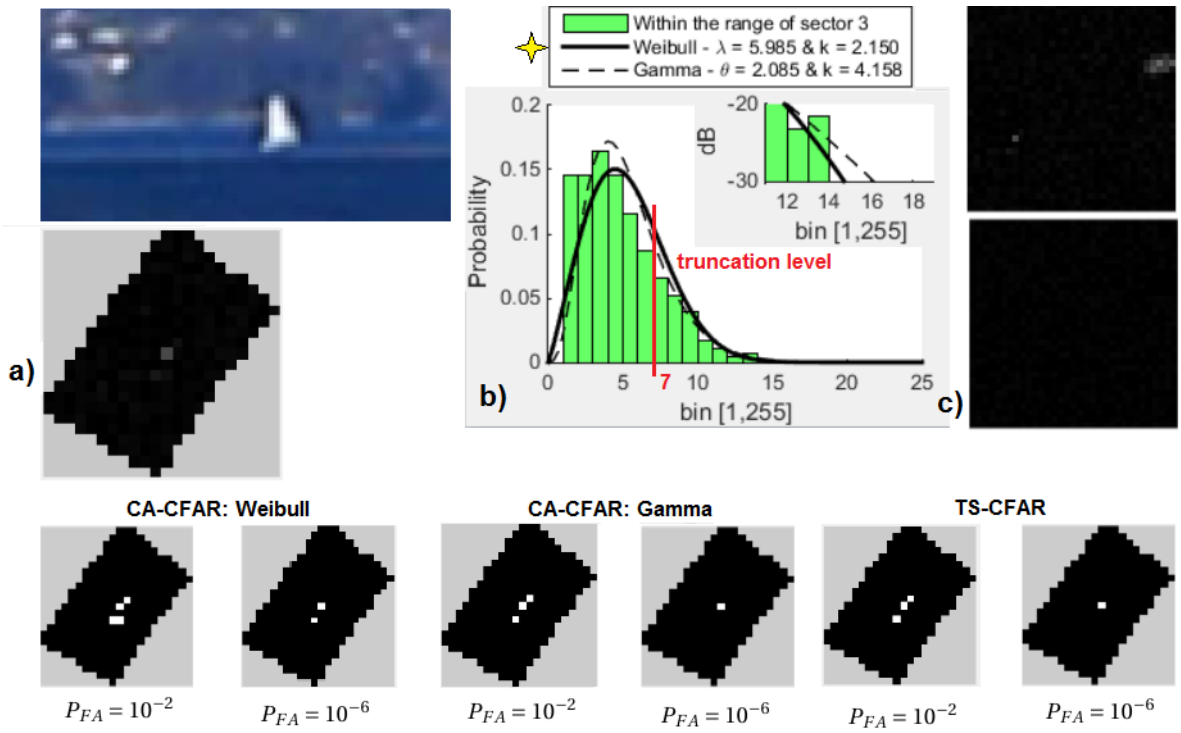

Figure 33: *Results from using CFAR on a) which is a sail boat at about 10 km range. The image above is captured by the Canon EOS 100D. Det data for the histogram in b) is extracted from a background window that is only containing clutter. Pixels with value 0 is removed from the data. The star denotes that the Weibull got the highest goodness to fit test score. The background window in the upper right corner c) contains both the sail boat and some land, and the image below is the truncated version.*

comparison is shown in figure 29. None of the algorithms perform very well, but they are able to detect both ships at $P_{FA} = 10^{-2}$. Since none of the algorithms were able to detect the ships at $P_{FA} = 10^{-6}$, the comparison is performed at higher probability of false alarm. The CA-CFAR that was modelled using the Weibull distribution was able to detect both ships even at $P_{FA} = 10^{-5}$, but since the other two did not detect the ships at that rate they are compared by using $P_{FA} = 10^{-3}$. The Weibull model is a better fit to the sea clutter as shown in figure 29 which explains why the CA-CFAR using this modell outperforms both the CA-CFAR and the TS-CFAR. The processed radar image at the time of the recording is also shown in d).

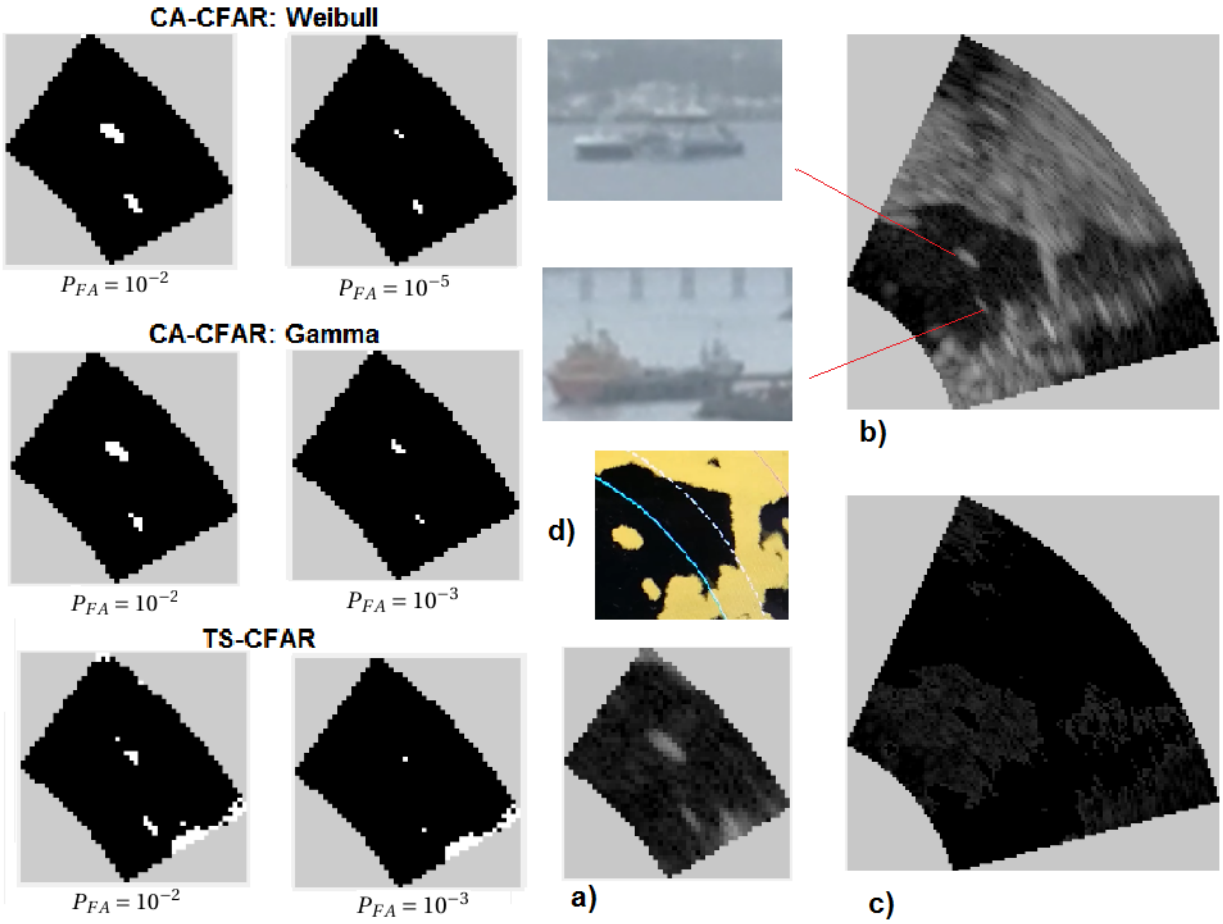

Figure 34: *Result of the comparison on the sector shown in a) of captured JRC data. An overview of the surroudings is shown in b) and the result of truncation using a truncation level of 44 is shown in c). A screen shot of the radar monitor at the time of the recording is shown in d). Notice that there is also water at the top of the image in b) which is the delta of Tromsdalen river.x*

5.3 Algorithm performance on a multiple target image

The TS-CFAR was originally designed for SAR images containing multiple targets [1], and for satellite SAR images ships often occupy few pixels as can be seen in figure 3. For dense target situations such in vessel traffic lanes or near fishing banks, many targets might occupy the same background window resulting in an inaccurate parameter estimation for conventional CFAR algorithms. We will in this section simulate such a situation by using a larger background window 63×63.

5.3.1 Experiment 4

We tested the algorithms on a fairly large sector, including 15 sub sectors in the algorithm, on the low resolution Sea-Hawk radar image. Moreover, the sector is at close range to the radar, within sector one in figure 22, and there are five ships in the sector. The truncation depth was chosen to be

20 % with a truncation level of 7. The result of the comparison is given in figure 35. The TS-CFAR is performing good even with such a large window size, but the CA-CFAR is struggling. The CA-CFAR algorithms fail to detect the ships at $P_{FA} = 10^{-6}$ and we will therefore compare them using $P_{FA} = 10^{-3}$. This is probably because several targets are within the background window which result in an overestimated mean. The TS-CFAR is performing better with a large background window and is actually detecting all the ships at $P_{FA} = 10^{-6}$. This is because the algorithm is not affected by the targets since they are truncated and no longer part of the statistics for the parameter estimation. A larger window size will result in more data for the estimation and a more accurate threshold for target detection. Although, if the window is too large the sea clutter statistics might variate significantly within the window because the depression angle relative to the radar is decreasing by increasing range as discussed in chapter 2.5. The TS-CFAR performs far from perfect as there are a lot of false alarms especially close to the radar. This is probably because the PDF does not fit the data very well as seen in figure 27 c). At $P_{FA} = 10^{-2}$ the TS-CFAR detects a wake that is most likely originating from the ship at the lower left corner. The wake can also be seen on the processed radar image. Some of the small dots seen in the processed image might be seagulls which is detected by the radar. These are recognized when looking at successive sweeps from their small target and fast and agile movement. They might have been detected which might explain the dots in the bottom and halfway to the ship at location a). The CA-CFAR using the Gamma PDF performs better than the CA-CFAR using the Weibull model which corresponds to the histogram for sector one in figure 27. Although, we have a suspicion that sector one is covering a too long range for the sea clutter statistics to be representative for the entire region. The tails for the two distributions are very similar for the histogram mentioned and the Gamma model got a better score for the goodness to fit test. Some variation can also be expected since the estimated histogram has a finite sample size and less is included in the sector at short range than long range, resulting in a less accurate estimation for pixels at short range.

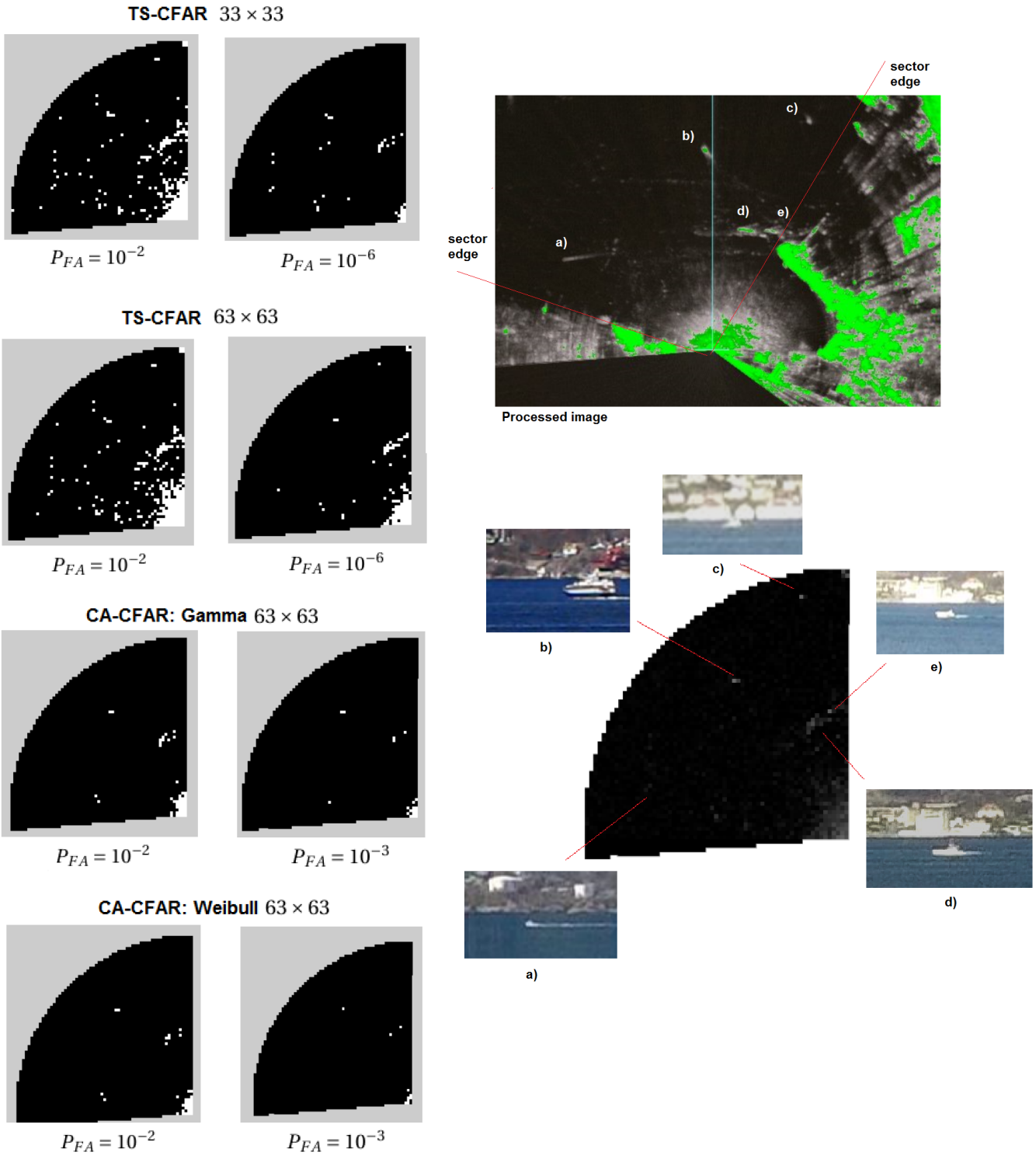

Figure 35: *Results from using CFAR on the sector shown to the right. There are five ships in the data a), b), c), d) and e), and the images were captured at the time of the recording using the Canon EOS 100D and a GoPRO camera. The ships are also seen on the processed image. The processed image has used scan to scan integration (3 integrations) to furhter enhance targets which can be seen in figure 23. Fast moving ships as a) is thus getting a trail. Notice that the lowest* P_{FA} *for the TS-CFAR is* 10^{-6} *and* 10^{-3} *for both the CA-CFAR*

Chapter 6

Discussion

In the previous chapter we have demonstrated that the TS-CFAR can be used on marine radars if the polar image is sectioned into regions of similar range. Furthermore, the statistical characterizations were summarized and the Gamma model was shown to sufficiently describe the sea clutter atleast for most cases, but not as well as the Weibull model. The results were presented and discussed, and in this chapter a more general and broader discussion will follow. As mentioned in the introductory chapter, one of the main goals for this thesis were to check whether the signal and statistical properties of marine radars are similar to satellite-borne SAR systems. Furthermore, we wanted to make a comparison between SAR and maritime radars to check whether there could be any cross-over applications by checking the properties. In this chapter our findings will be discussed.

6.1 Marine radars and SAR comparison

For SAR imagery the incidence angle is not changing considerably from one end of the image to the other as shown in figure 2. Marine radars operate from an entirely different perspective which is often referred to as from low grazing angles, and will of course have greatly varying incidence angle across the image. From the marine radar perspective the term depression angle is often used. In chapter 2.5, we summarized the background theory of why we expected that the mean brightness of the sea clutter would decrease by increasing range and decreasing depression angle. This hypothesis was tested by separating sections of the image into different regions by increasing range as shown in figure 22 and figure 24. Data was extracted from each section and histograms were plotted for each sections and for data captured by each radar. Our results show that the mean brightness decrease with increasing range as expected for the high resolution data captured by the

Sea-Hawk radar, but that it is increasing by increasing range for the low resolution Sea-Hawk data, which was not expected. This is not true from sector one to sector two for the low resolution image, where the mean brightness is decreasing at increasing range as expected. Sector one for the low resolution image covers about the same range as the three first sectors for the high resolution image, and sector two for the low resolution image can be compared with sector four for the high resolution image. Thus, the mean brightness for both images decrease for increasing range until atleast about 5 km. Furthermore, the gain is automatically adjusted in marine radars to compensate for signal attenuation at increasing range as summarized in chapter 2.6.2. We expect that the gain control is overcompensating the level of attenuation in the Sea-Hawk image, which might explain the mean brightness increasing at long range. By plotting the noise distribution for the two radar images, and comparing it with the distribution of clutter in the different sectors, it is evident that at considerable range the backscatter from the sea is so weak that the clutter can be considered pure thermal noise and radar interference. A good model for the clutter must therefore be able to estimate the distribution of pure noise as well as the distribution of sea clutter and noise combined. As summarized in chapter 2.4.2, thermal noise and sea clutter at low sea states both follow the Gaussian probability density function, which means that the sea clutter can therefore be considered similar to noise with added power. Moreover, for non-coherent radars with linear detectors a Gaussian PDF will be transformed to a Rayleigh in the local oscillator. The Rayleigh distribution fits the data well in all cases where the data is extracted from sectors at long range such as sector two, three and four for the low resolution Sea-Hawk image and sector four for the high resolution Sea-Hawk image. This is shown in figure 27 and figure 26 respectively. This strengthens our theory that the clutter at these sectors are mainly noise. The Rayleigh fit the noise distribution for the low resolution Sea-Hawk image well, but fail to fit the tail for the distribution of noise from the high resolution Sea-Hawk image. This is most likely because of the bright streaks seen clearly in the blocked sector of the high resolution image in figure 24, which we expect is radar interference. This effect is much stronger in the high resolution image than the low resolution Sea-Hawk image which is probably because the gain was adjusted higher for the latter. The clutter distribution in sector four for the high resolution image can therefore not only be noise, but must be a combination of noise, sea clutter and radar interference. Because the noise seems to fit the Rayleigh distribution well we expect that the Sea-Hawk radar has a linear detector which means that the signal is proportional to amplitude. Although, we were not able to get this confirmed by Sea-Hawk. A summary of envelope detectors were given in chapter 3.1.1. The JRC radar is a coherent radar and the envelope detector is a linear detector as was summarized in chapter 3.1.2. The data is therefore also proportional to the amplitude. The Rayleigh PDF is a good fit for the data ex-

tracted from the JRC as expected from the amplitude of sea clutter at low sea states. This is shown in figure 29. Furthermore, the goodness of fit test scores in figure 30 confirms that the Rayleigh is the best fit for the JRC data. For SAR, the speckle is Gaussian distributed with zero mean for the I- and Q component as also mentioned in chapter 2.4.3, and the amplitude is Rayleigh distributed [3], just as it is for marine radars with linear detectors. Although, it is only for coherent radars that the detection is truly linear as it is only for such radars that the phase information is kept [11]. For a coherent radar with a in-phase (I) and quadrature-phase (Q) component, the best estimate for the mean radar cross section (σ) is intensity, which is the square of the amplitude and thus power [3]. This follows from taking the maximum likelihood estimate of σ [3]. In SAR imagery the intensity image is therefore often used, which also proves to be the best estimate for the average of L multi-looked images, the average of L multi-looked amplitude images is an inferior estimating of σ [3]. Multi-looking is performed to reduce the speckle noise in SAR imagery [3]. For multi-looked intensity images the Gamma model is a good fit as mentioned in chapter 2.7.5. Scan to scan integration in marine radars, which is summarized by *J.N. Briggs* [6], might be equivalent to multi-looking in SAR. Further research could be done, investigating if the sea clutter in marine radars follow the Gamma distribution when the data is scan to scan integrated. For the reasons mentioned, a detection algorithm developed for SAR must use a probability density function that is flexible enough to both estimate low sea states and noise, and to estimate high sea states if it is to be used on a marine radar. Furthermore, the algorithm should be able to perform new parameter estimations at different regions of the image because the clutter statistics are likely to change throughout the image. This is not only because of the changing incidence angle and mean brightness, but also because the backscatter will be different when the radar is facing the wind as it is when the radar is looking down the wind and the sea states will variate in different regions. This was summarized in chapter 2.4.2. We have performed a model comparison between the Weibull, the Gamma, Log normal and the Rayleigh. We found that the Weibull PDF fit the clutter best for most of the data. This is probably because it is flexible enough to both describe thermal noise which is known to be Rayleigh distributed, and to describe the clutter when it is distributed with a longer tail. The Rayleigh distribution is of course just a special case of the Weibull distribution when the shape parameter k equals to 2. The Gamma distribution did also fit the data well for the low resolution Sea-Hawk image at long range, but not equality well for the high resolution image except for sector one at closest range. In sector two the Gamma model is far from optimal, but in the same sector with a higher sea state the Gamma model proved to be the best fit, as shown in figure 31. This result highlights that the Gamma model may be a good model to estimate the sea clutter at higher sea states. We were not able to do this because such data was not available to us,

but this is a possible study for future research. The Log normal PDF was the best fit for data at short range for the low resolution Sea-Hawk data, but this might also be because the histogram in sector one might be a mixture, since the length of the sector might have been too long. It is known that spatial resolution affects the received clutter statistics. If the resolution cell is no longer very large compared to the distribution of scatterers the central limit theorem no longer is valid, as was discussed in chapter 2.4.2, and the distribution of capillary waves will no longer be Gaussian distributed. This is also the case for sea clutter at higher sea states.

A comparison between SAR and marine radars would not be complete without having mentioned resolution. One of the main differences between the resolution of a marine radar and SAR is that the azimuth resolution greatly diminishes at increasing range for marine radars as shown in figure 6. An example is given by looking at figure 23 c). The sail boat is the same as b) but cut into the image from a sweep earlier in time. The sail boat in b) is larger even though it is the same boat, which might illustrate that the azimuth resolution cell is larger at this point. The boat is also large compared to the other boats at closer range even though many of those boats are larger. Some of the other boats can be seen in figure 35. Especially ship b) in that figure is much larger than the sail boat. Furthermore, as the range setting is changed on the radar the pulse repetition frequency will also change. For non-coherent radars the maximum range resolution is directly dependent on pulse repetition frequency because two target can not be separated from each other if the leading edge from the transmitted pulse is mixed with the trailing edge of the previous pulse. This was summarized in chapter 2.2 and chapter 2.1 respectively. For coherent radars the range resolution is directly dependent on transmitted bandwidth as shown in equation 17. A SAR is a coherent radar that uses chirp frequency modulation and is for that reason most comparative to coherent marine radars such as the JRC JMR solid state radar. Although, it may prove difficult to extract the I- and Q component from the marine radar, and thus be able to use the phase information. A SAR algorithm that takes advantage of the phase information will for that reason be difficult to use on a marine radar because it might prove difficult to extract the data, which probably is proprietary information for most radar manufacturers. A block diagram of a typical marine doppler radar was shown in figure 15. To end the comparison we will also mention the Sea-Hawk radar and the fact that it is a polarimetric radar. Most radar use horizontal polarization, but the Sea-Hawk radars is a new generation state-of-the-art radars that uses both horizontal and circular polarization. We have used horizontal polarization in our comparison. The radar is able to combine the polarizations in for instance $\frac{HP+CP}{2}$ and $\frac{HP+CP}{2}$, or use only horizontal polarization (HP) or circular polarization (CP). Circular polarization is according to Sea-Hawk better under heavy rain. Future

research might be possible in trying to see if any SAR polarimetric applications can be used on marine polarimetric marine radars such as the Sea-Hawk radars. There is a lot of current SAR research on these Hybrid SAR systems, also known as compact polarimetry, with circular send and linear receive. In *Nord et al* [25] a comparison of such compact polarimetric SAR modes is performed. Another interesting subject to research, could be comparing marine radar images that are scan to scan correlated, with multi-looking SAR radar images. In *Briggs* [6] scan to scan correlation in marine radars is summarized. We did not have time in our study to perform such a comparison.

6.2 The TS-CFAR performance

In the previous chapter we demonstrated that the TS-CFAR algorithm developed for SAR images could be successfully used on marine radar images. We have thus performed a first cross-over for a SAR application to the marine community. The comparison was performed on polar images extracted from different range sectors, different radars and different resolution. By doing this we were able to make a comparison under different conditions. The comparison can be separated into four different experiments whose discussion follows. We chose to compare the TS-CFAR with the CA-CFAR firstly to make the comparison simple and secondly because we consider the CA-CFAR to be the most conventional and simplest CFAR algorithm used on marine radars. The CA-CFAR performance is also very intuitive as it is only using the mean intensity of the background window for the parameter estimation for the underlying PDF , and the threshold decision. Furthermore, the TS-CFAR used in this thesis is also using the mean intensity of the truncated background window, which means that the two algorithms are simple to compare and the only difference is the truncation with the truncated version of the PDF. Moreover, we used two CA-CFAR with different underlying PDF, one using the Weibull distribution and one using the Gamma distribution. By doing this we were able to perform an additional model comparison between the two models and we could easily see if the performance was not as expected. By using the CA-CFAR with the Gamma model we were also able to compare the two algorithm independent of the underlying model. This is because the TS-CFAR is also using the Gamma distribution, the truncated version. A summary of the theory behind CA-CFAR and TS-CFAR were given in chapter 2.7.5. When possible, we compared the three algorithms with a high $P_{FA} = 10^{-2}$ and with a low $P_{FA} = 10^{-6}$. According to *J. N. Briggs* [6], a radar should use a $P_{FA} < 10^{-6}$ in order to optimize perception on a radar monitor. We chose to also compare the algorithm at a higher P_{FA} to see how the algorithm performs on a wide P_{FA} range. It also highlights any possible properties. For instance, it turned out that the TS-CFAR is able to clearly detect the wake a $P_{FA} = 10^{-2}$, but it is not detecting it at $P_{FA} = 10^{-6}$.

Fore pure ship detection the wake is undesirable, but for another application it could be desirable to detect the wake. It depends on the purpose of the application. The TS-CFAR performed better than the CA-CFAR for all instances where there either were several targets such as in experiment four or when the resolution of the image was so high that the target occupy several pixels such as in experiment one. This is because targets contaminate the background window for the CA-CFAR resulting in a overestimated mean which again result in a threshold at a higher level. For the TS-CFAR the targets are truncated and do not contribute to the estimation of the mean. Experiment two was performed to test the algorithms on an entirely different situation than experiment one. In experiment one the target was large and occupied several pixels, for experiment two the target was very small and weak and barely occupied a few pixels. There was no other targets nearby which demonstrated that the TS-CFAR had no advantage on such a situation and only the underlying PDF made a difference. For that reason, both the CA-CFAR modelled using the Gamma model and the TS-CFAR got the same result. Experiment three was decided to be a challenge for the algorithms as there were so little space and so little clutter available for estimating the parameters, as seen in figure 28. Furthermore, we wanted to also test the algorithm performance on the JRC data. The sector is surrounded by land clutter and we therefore decided to use a small background windows at 13×13. Since the window was so small the background window for the CA-CFAR was not contaminated at the essential cell under test (CUT), the cells that were targets. The truncation just proved to be a disadvantage for the TS-CFAR, because less pixels were available for the parameter estimation because of truncation. The last experiment, experiment four, was to compare the algorithms at a situation where the TS-CFAR was expected to perform better than the CA-CFAR. Opposite to experiment three, the window sizes were chosen to be large such that the CA-CFAR would have an obvious disadvantage. This demonstrated how the TS-CFAR perform on a situation it was designed for and it proves to greatly outperform the CA-CFAR. Experiment one, two and three demonstrates that the Weibull was the better model for the sea clutter for these sectors and that the model comparison shown in figure 26 and figure 27 seems to be accurate for the corresponding sectors. Experiment four also corresponds to the histogram for sector one in figure 27 c). The Weibull has a tail that is further to the right and will for that reason detect less targets at an increasing P_{FA}. These conclusions can be made by comparing the CA-CFAR using the Weibull model by the CA-CFAR using the Gamma model.

6.3 Limitations

All science has its limitations and we should summarize them. One obvious limitation to our model comparison is that we have only compared the models for sea clutter at low sea states. A more complete study should also compare the models for sea clutter at higher sea states. Furthermore, our data may contain some amount of contamination as it was not possible to be sure that there were absolutely no contamination in our sea clutter data, even though care was taken to limit this amount. We also made sure to extract enough data for each sector such that the amount of sea clutter compared to the amount of contamination would be very high. For sectors at close range this was not easy, especially on the low resolution image because the amount of targets was so large in this sector. For the end of sector three and sector four for the low resolution image we were not able compare the raw data with processed data since we had no processed data at that range. We also did not have processed data for the high resolution Sea-Hawk image, but the resolution was so good that we don't think we missed any targets of significant size.

Chapter 7

Conclusion

In this thesis we have showed where to extract raw data from marine radars, and how this can be done using equipment such as a scan streamer. This was a formidable task and by our work we are confident that we are able to help future project facing this difficulty. We have summarized SAR and marine radar properties to highlight both the similarities and differences. Furthermore, we have experienced that extracting the I- and Q component on a marine radar will probably not be an easy task and might need approval from the radar manufacturer. SAR applications based on phase information will therefore not be possible to use on marine radars, unless this information becomes available. We have figured out through our investigation that the demodulated output voltage can either be proportional to amplitude, power, or it is logarithmically amplified. By extracting sea clutter data from sectors at increasing range we have confirmed that the sea clutter statistics is changing with respect to range to the radar. Moreover, the model comparison led us to the conclusion that the Gamma model can be used to sufficiently model sea clutter, but that the Weibull model is a better fit, atleast for low sea states. The Gamma model was found to be the best model describing sea swell for our high resolution Sea-Hawk data, and we propose that further research can be done to check whether the Gamma PDF is a good model for high sea states. We have demonstrated that the TS-CFAR can be used on marine radars which is a first demonstration of possible cross-over for application from SAR to marine radars, or opposite. Our demonstration shows that the TS-CFAR can improve the detection capabilities of a marine radar for high resolution and for multiple target situations. We have also showed that the sliding window technique using a 2-D background window is possible on polar images.

Appendix A

Cumulative distribution functions (CDF)

For a random variable $X(\zeta)$, the cumulative distribution function $F_X(x)$ is defined as the probability that the outcome ζ has a value between $-\infty$ and x. This outcome (ζ) can be any outcome in the underlying sample space. Mathematically the CDF is defined as [12]:

$$F_X(x) = P_X[< -\infty, x]]$$

The properties of $F_X(x)$ are the following[12]:

1) $F_X(\infty) = 1$ and $F_X(-\infty) = 0$

2) $x1 \leq x2 \rightarrow F_X(x1) \leq F_X(x2)$

3) F_X is continuous from the right

From these properties it follows that:

$$F_X(b) - F_X(a) = P[a < X \leq b]$$

Here follows some cumulative distribution functions for different random variables [12]:

Gaussian:

$$F_X(x) = \frac{1}{2} + erf\left(\frac{x-\mu}{\sigma}\right) \tag{47}$$

Where μ is the mean and σ is the standard deviation

Log-normal:

$$F_X(x) = \frac{1}{2} + \frac{1}{2} erf\left(\frac{\ln x - \mu}{\sqrt{2}\sigma}\right) \tag{48}$$

where $erf(x) = \frac{1}{2\pi}\int_0^x e^{-\frac{1}{2}t^2}$, μ is the mean and σ is the standard deviation

Weibull:

$$F_X(x) = 1 - \exp\left[\left(\frac{x}{k}\right)^k\right] \tag{49}$$

for $x \geq 0$ where k is the shape parameter.

Gamma:

$$F_X(x) = \frac{1}{\Gamma(k)}\gamma\left(k, \frac{x}{\theta}\right) \tag{50}$$

for shape parameter k and scale parameter θ The complete Γ and the incomplete gamma functions γ are defined as follows:

$$\Gamma(x) = \int_0^\infty x^{z-1}e^{-x}dx \tag{51}$$

$$\gamma(a,b) = \int_0^b y^{a-1}e^{-y}dy \tag{52}$$

Appendix B

Probability density functions (PDF)

The probability density function is as its name suggest a function for the probability of an outcome ζ of a random variable $X(\zeta)$ to get a certain value x. The PDF is the derivative of the CDF as long as the CDF is continuous and differentiable [12].

$$f_X(x) = \frac{dF_X(x)}{dx}$$

B.1 Gaussian PDF

The most common PDF is probably the *Gaussian* (normal) PDF, given by:

$$f_X(x) = \frac{1}{\sqrt{2\pi\sigma^2}}\, exp\left[-\frac{1}{2}\left[\frac{x-\mu}{\sigma}\right]^2\right]$$

Where :

1) $x \in \langle -\infty, +\infty \rangle$

2) μ is the mean, defined as [12]:

$$\mu \triangleq \int_{-\infty}^{\infty} x\, f_X(x)dx = E\{X\}$$

3) σ is the standard deviation ($\sigma > 0$), and σ^2 is the variance defined as [12]:

$$\sigma^2 \triangleq \int_{-\infty}^{\infty} (x-\mu)^2\, f_X(x)dx = Var\{X\}$$

Below is a plot of two *Gaussian* PDF's using MATLAB with equal mean, but with different variance:

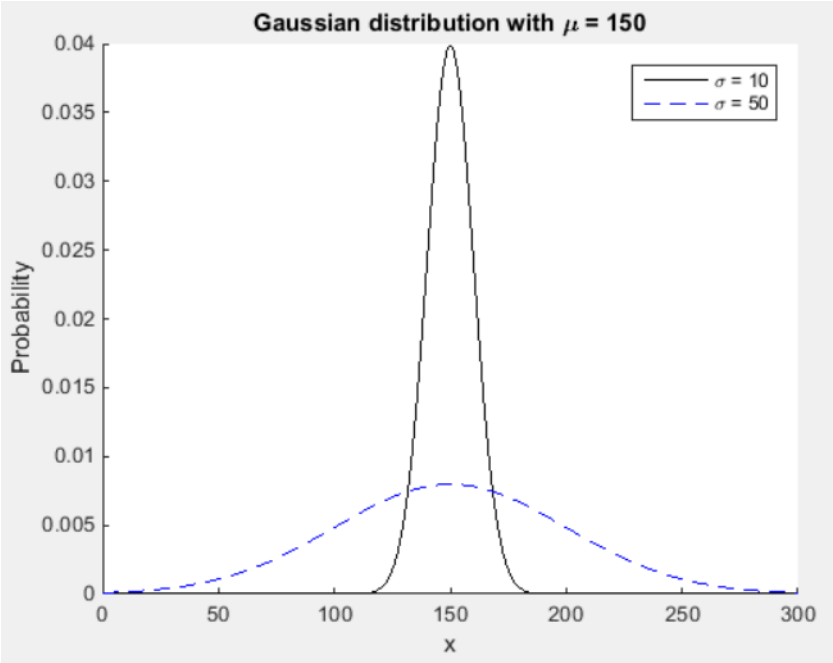

B.2 Log-normal PDF

The logarithmic version of the *normal* (Gaussian) distribution is the *log-normal* distribution. The random variable have a normal distribution

$$f_X(x) = \frac{1}{x\sqrt{2\pi\sigma^2}}\, exp\left[-\frac{1}{2}\left[\frac{ln(x) - x_m}{\sigma}\right]^2\right]$$

Where :

1) $x \in \langle 0, +\infty \rangle$

2) x_m is the median. The *scale parameter* μ is given by the relation:

$$\mu = exp(x_m)$$

3) The mean is as follows [6]:

$$E\{X\} = exp\left(\frac{\sigma^2}{2}\right)\; x_m = exp\left(\mu + \frac{\sigma^2}{2}\right)$$

4) σ is the *shape parameter*. The variance is given by:

$$var\{X\} = exp[2(\mu + \sigma^2)] \; - \; exp(2\mu + \sigma^2)$$

Below is a plot of three *log-normal* PDF's using MATLAB with equal *scale parameters*, but different *shape parameters*:

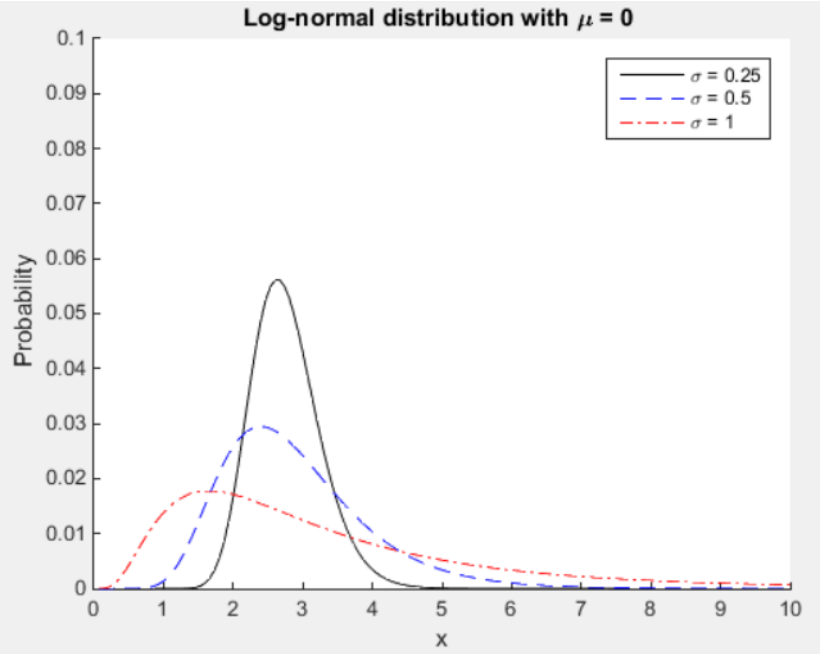

B.3 Weibull PDF

The Weibull has been used to model sea clutter since the eighties [6]. It has the property that it equals the exponential distribution with *shape parameter* k=1 (c=0.5), and the Rayleigh distribution with *shape parameter* $k = 2$ and *scale parameter* $\lambda = \sqrt{2}\sigma$, where σ is the scale parameter for the Rayleigh distribution.

$$f_X(x) = \frac{k}{\lambda}\left(\frac{x}{\lambda}\right)^{k-1} \; exp\left(-\frac{x}{\lambda}\right)^k$$

By letting $\bar{\sigma} = \lambda^k$, and $2c = k$, we get the form used in [6] and which seems to be more common for marine target detection.

$$f_X(x) = \frac{2c}{\bar{\sigma}} x^{2c-1} \; exp\left(-\frac{x^k}{\bar{\sigma}}\right)$$

Below is a plot of four *Weibull* PDF's using MATLAB with equal *scale parameters*, but different *shape parameters*. Notice that with $k = 1$ the distribution is an exponential, and with $k = 2$ it is a Rayleigh.

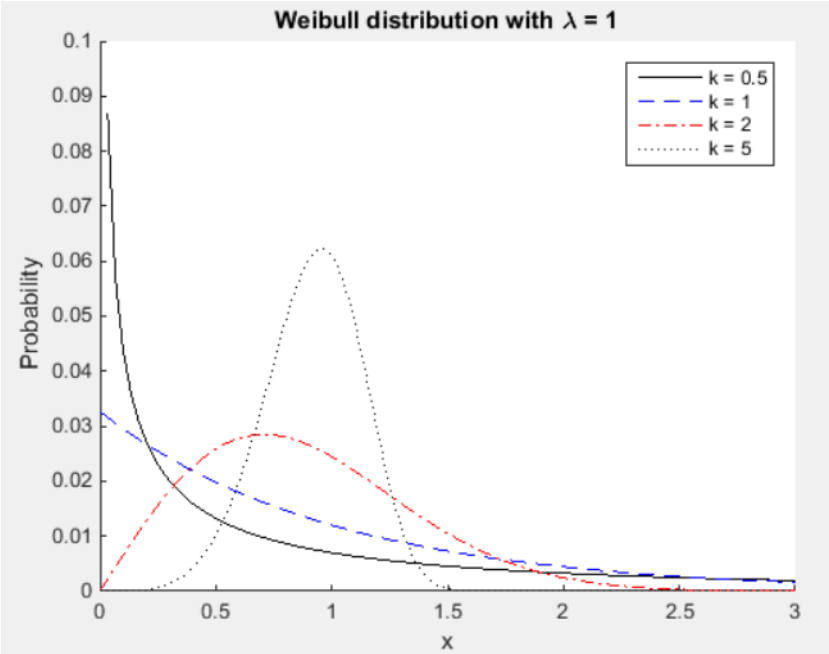

The following values have been found empirically to describe different sea states [6]:

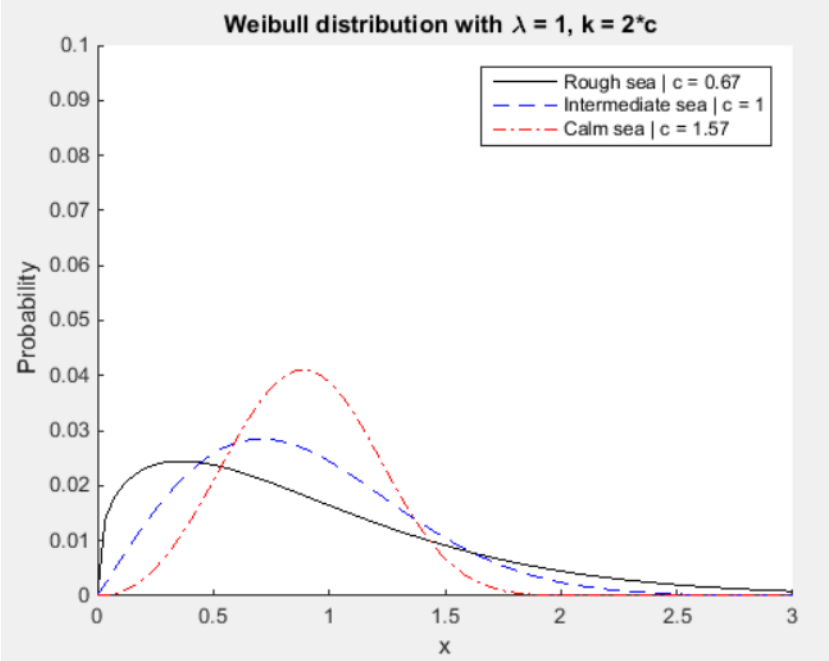

B.4 Gamma PDF

The Gamma distribution is frequently used in the SAR community to model multi-looked intensity (MLI) radar images [3]. The general form is given below, where k is the shape parameter and θ is the scale parameter:

$$f_X(x) = \frac{1}{\Gamma(k)\theta^k} x^{k-1} exp\left(-\frac{x}{\theta}\right) \tag{53}$$

Where $\Gamma(k)$ is the gamma function defined as $\Gamma(k) = \int_0^\infty y^{k-1} exp(-y)dy$.

For SAR images it is usual to let the shape parameter k, or also called the order parameter [3], be

defined as the equivalent number of looks L. Furthermore, the relation $\theta = \frac{\mu}{L}$ is used such that the formula for the gamma distribution in these terms will be as shown below [3]:

$$f_X(x) = \left(\frac{L}{\mu}\right)^L \frac{x^{L-1}}{\Gamma(L)} exp\left(-\frac{Lx}{\mu}\right) \tag{54}$$

Bibliography

[1] D. Tao, S.N. Anfinsen, and C. Brekke. Robust CFAR Detector based on Truncated Statistics in Multiple Target Situations. *IEEE Transactions on Geoscience and Remote Sensing*, 2014.

[2] A. Bole, A. Wall, and A. Norris. *Radar, AIS and Target Tracking for Marine Radar Users: Radar and ARPA Manual*. Elsevier, Amsterdam, third edition, 2011.

[3] C. Oliver and S. Quegan. *Understanding Synthetic Aperture Radar Images*. SciTech Publishing, Raleigh, 2004.

[4] J.H McClellan, R.W Schafer, and M. A. Yoder. *Signal Processing First*. Pearson, Upper Saddle River, 2003.

[5] D.K. Barton. *Radar Equations for Modern Radar*. Artech House, Norwood, US, 2012.

[6] J. N. Briggs. *Target Detection by Marine Radar*. The Institution of Engineering and Technology, London, 2004.

[7] J. van Zyl and Y. Kim. *Synthetic Aperture Radar Polarimetry*. John Wiley & Sons, Hoboken, New Jersey, 2011.

[8] C. Elachi and J. van Zyl. *Introduction to the Physcis and Techniques of Remote Sensing*. John Wiley & Sons, Hoboken, New Jersey, 2006.

[9] SOLAS - International Convention for the Safety of Life at Sea . *Lloyd's Register Rulefinder 2005 – Version 9.4*, 2005.

[10] N. Kjerstad. *Elektroniske og akustiske naviasjonssystemer: for maritime studier*. Tapir Akademisk Forlag, Trondheim, 4 edition, 2010.

[11] J. L. Eaves and E. K. Reedy. *Principles of Modern Radar*. Van Nostrand Reinhold, New York, 1987.

[12] H. Stark and J.W. Woods. *Probability, Statistics, and Random Processes for Engineers*. Pearson, Edinburgh, fourth edition, 2012.

[13] M. Sekine and Y. Mao. *Weibull Radar Clutter*. Peter Peregrinus Ltd, London, 1990.

[14] E. Jakeman and P.N. Pusey. A Model for Non-Rayleigh Sea Echo. *IEEE Transactions on Antennas and Propagation*, 24(6), 1976.

[15] Long Cai, Xiaochuan Ma, Qi Xu, Bin Li, and Shiwei Ren. Performance Analysis of Some New CFAR Detectors under Clutter. *Journal of Computers*, 6(6), 2011.

[16] D.J. Crisp. *The State-of-the-Art in Ship Detection in Synthethic Aperture Radar Imagery*. DSTO Information Sciences Laboratory, Edinburgh, South Australia, 2004.

[17] H. Rohling. Radar CFAR Thresholding in Clutter and Multiple Target Situations. *IEEE Transactions on Aerospace and Electronic Systems*, AES-19(4), 1983.

[18] M. Ihlen. Automatic Detection for MTI Processed Radar Signals. *Norwegian University of Science and Technology Department of Electronics and Telecommunications*, 2011.

[19] Y. Cui, G. Zhou, J. Yang, and Y. Yamaguchi. On the Iterative Censoring for Target Detection in SAR Images. *IEEE Geoscience and Remote Sensing Letters*, 8(4), 2011.

[20] S. Thedoridis and K. Koutroumbas. *Pattern Recognition*. Elsevier Science & Technology, Oxford, United Kingdom, 4 edition, 2008.

[21] Radar basics. `http://www.radartutorial.eu/08.transmitters/Pseudo-coherent%20Radar.en.html`, 2017. [Online; accessed 01-Aug-2017].

[22] Scanstreamer technical data. `https://dspnor.com/products/scanstreamer/scanstreamer-technical-data/`, 2017. [Online; accessed 19-July-2017].

[23] Eurocontrol standard documents for surveillance data exchange category 240. *European organisation for the safety of air navigaton*, 2009.

[24] E. Conte, M.Longo, and M. Lops. Modelling and simulation of non-Rayleigh radar clutter. *IEE Proceedings-F*, 138(2), 1991.

[25] M.E. Nord, T. L. Ainsworth, J. Lee, and N. J. S. Stacy. Comparison of Compact Polarimetric Synthetic Aperture Radar Modes. *IEE Transactions on Geoscience and Remote Sensing*, 47(1), 2009.